Neuron

CellPress

Review

Whole-Brain Profiling of Cells and Circuits in Mammals by Tissue Clearing and Light-Sheet Microscopy

Hiroki R. Ueda,[1,2,*] Hans-Ulrich Dodt,[3,4] Pavel Osten,[5] Michael N. Economo,[6] Jayaram Chandrashekar,[7] and Philipp J. Keller[7]

[1]Department of Systems Pharmacology, The University of Tokyo, Tokyo 113-0033, Japan
[2]Laboratory for Synthetic Biology, RIKEN BDR, Suita, Osaka 565-0871, Japan
[3]Department of Bioelectronics, FKE, Vienna University of Technology-TU Wien, Vienna, Austria
[4]Section of Bioelectronics, Center for Brain Research, Medical University of Vienna, Vienna, Austria
[5]Cold Spring Harbor Laboratories, Cold Spring Harbor, NY 11724, USA
[6]Department of Biomedical Engineering, Boston University, Boston, MA, USA
[7]Janelia Research Campus, Howard Hughes Medical Institute, Ashburn, VA, USA
*Correspondence: uedah-tky@umin.ac.jp
https://doi.org/10.1016/j.neuron.2020.03.004

Tissue clearing and light-sheet microscopy have a 100-year-plus history, yet these fields have been combined only recently to facilitate novel experiments and measurements in neuroscience. Since tissue-clearing methods were first combined with modernized light-sheet microscopy a decade ago, the performance of both technologies has rapidly improved, broadening their applications. Here, we review the state of the art of tissue-clearing methods and light-sheet microscopy and discuss applications of these techniques in profiling cells and circuits in mice. We examine outstanding challenges and future opportunities for expanding these techniques to achieve brain-wide profiling of cells and circuits in primates and humans. Such integration will help provide a systems-level understanding of the physiology and pathology of our central nervous system.

The beginning of the 20th century saw the birth of two technologies: tissue clearing and light-sheet microscopy. The earliest report on tissue clearing of opaque biomedical samples, which appeared in 1911 in Leipzig, was by the German anatomist Walter Spalteholz. He tried to make human hearts transparent to study their vascular system (Spalteholz, 1911). Using hydrophobic tissue-clearing reagents (Wintergrünöl) such as methyl salicylate and benzyl benzoate on dehydrated specimens, he succeeded in visualizing macroscopic structures in transparent samples for the first time. However, without a technology like light-sheet microscopy, it was not possible to quantify his findings. So even this key advance brought only some qualitative insights into human anatomy. Not far from Leipzig, Austrian chemist Richard A. Zsigmondy and German physicist Henry Siedentopf, working in Jena, developed the first light-sheet microscope, the Ultramicroscope (Siedentopf and Zsigmondy, 1902). Unlike Spalteholz, Zsigmondy was looking for very small things (Ultramikronen), colloidal particles in solution, which he tried to quantify. In principle, it would have been possible to integrate these two technologies more than 100 years ago, but at that time, it would not have led far. Light sheets traversing cleared specimens might create optical sections if one looks at the specimen at the correct angle, but these images still had to be recorded. Most importantly, a three-dimensional (3D) model of the specimen must be reconstructed digitally. Without concurrent inventions of electronic cameras and computers, even a hypothetical encounter of Spalteholz and Zsigmondy would not have produced the same impact that these methods have recently achieved.

Approximately 90 years after these seminal works, the first relevant step toward integration of tissue clearing and light-sheet microscopy was made by Arno Voie and colleagues (Voie et al., 1993). They designed a modern version of light-sheet microscopy (orthogonal-plane fluorescence optical sectioning microscopy [OPFOS]), based on lasers and digital camera technology. After clearing the bony structure of the inner ear using EDTA and Spalteholz's hydrophobic tissue-clearing reagents (methyl salicylate and benzyl benzoate), Voie and colleagues performed the first fluorescence optical imaging of a tissue-cleared biological specimen, an excised guinea-pig cochlea labeled with fluorescein (Voie et al., 1993). They recorded the images with a charge-coupled device (CCD) camera and successfully reconstructed the spiral in the inner ear with rudimentary homemade 3D reconstruction software. The approach unfortunately remained largely unnoticed by the broader scientific community for nearly two decades. Light-sheet microscopy rapidly gained momentum in biological imaging in the early 21st century, with applications in diverse fields including microbial oceanography, developmental biology, and neuroscience (Dodt et al., 2007; Fuchs et al., 2002; Holekamp et al., 2008; Huisken et al., 2004). In particular, the work by Ernst Stelzer and colleagues sparked a renewed interest in light-sheet microscopy (Huisken et al., 2004). They reconstructed largely transparent living biological samples, including Medaka fish embryos. Despite the success of this approach for developmental biology, it remained restricted to naturally transparent samples. The first use of light-sheet imaging on neural tissues artificially rendered transparent was made by Hans-Ulrich Dodt and colleagues (Dodt

et al., 2007). They took advantage of hydrophobic tissue-clearing reagents, benzyl alcohol and benzyl benzoate (BABB), that were originally developed by Andrew Murray and Marc Kirschner around 1989 and first applied to fluorescent- and peroxidase-based whole-mount immunocytochemistry of *Xenopus* oocytes and embryos (Dent et al., 1989). Combining this clearing method with ultramicroscopy and image processing enabled the visualization of neuronal networks at the resolution of neural dendrites in whole mouse brains (Dodt et al., 2007). A different set of organic solvents—DBE (dibenzyl ether) and/or THF (tetrahydrofuran) and dichloromethane (DCM)—were combined in 3D imaging of solvent-cleared organs (3DISCO) to better preserve the fluorescence of GFP during the clearing process (Becker et al., 2012, 2014; Ertürk et al., 2012, 2014). Since then, various other hydrophobic tissue-clearing reagents with different attributes have been developed to support various applications, including ultimate DISCO (uDISCO) (Pan et al., 2016), immunolabeling-enabled DISCO (iDISCO) (Belle et al., 2014; Renier et al., 2014), iDISCO+ (Renier et al., 2016), FluoClearBABB (Schwarz et al., 2015), ethyl cinnamate (ECi) (Klingberg et al., 2017), free-of-acrylamide SDS-based tissue clearing (FASTClear) (Perbellini et al., 2017), polyethylene glycol (PEG)-associated solvent system (PEGASOS) (Jing et al., 2018), variable domain of heavy chain antibodies (nanobodies) DISCO (vDISCO) (Cai et al., 2018), multiscale architectonic staining of human cortex (MASH) (Hildebrand et al., 2018), and stabilized DISCO (sDISCO) (Hahn et al., 2019).

Clearing methods that use water-soluble reagents (hydrophilic tissue-clearing methods) are better at preserving the fluorescence of fluorescent proteins and are less toxic compared with approaches that use organic reagents. Pioneering works on hydrophilic tissue-clearing methods were conducted by Russian physicist Valery V. Tuchin and colleagues (V.V. Bakutkin et al., 1995, Int. Soc. Optic. Photon., conference; Tuchin, 2007). They found that aqueous solutions of various hydrophilic chemicals had high refractive indices (RIs), a property believed to be important for tissue clarity. The RI of a certain material is defined as the ratio of the speed of light in a vacuum to that in the material. These high-RI solutions included X-ray contrast agents (Trazograph), a series of alcohols (polyethylene glycol, glycerol, and propylene glycol), sugars (glucose and dextran), and dimethyl sulfoxide (DMSO) (V.V. Bakutkin et al., 1995, Int. Soc. Optic. Photon., conference; A.N. Bashkatov et al., 1999, Int. Soc. Optic. Photon., conference; V.V. Tuchin et al., 1999, Proc. SPIE, conference; Tuchin et al., 1997, 2002; Xu et al., 2003; Zimnyakov et al., 1996, Int. Soc. Optic. Photon., conference). Around the same time, Chance and colleagues discovered the RI matching effect of a series of sugars (mannitol, fructose, sucrose, and glucose) and alcohols (propanediol and methanol) (Chance et al., 1995; Liu et al., 1996). A different cocktail—FocusClear, which contains another X-ray contrast agent (diatrizoate acid) and a detergent (Tween 20)—was used by Chiang and colleagues for whole-brain imaging of cockroach using a confocal microscope (Chiang et al., 2001). In 2011, Atsushi Miyawaki and colleagues developed the hydrophilic tissue-clearing method Sca*l*e, which hyperhydrates and delipidates mouse brains with urea-based reagents and a detergent, respectively, resulting in semi-transparent mouse brains (Hama et al., 2011). This clearing approach substantially enhanced the effective imaging depth of two-photon microscopy in adult brain tissue but provided insufficient clearing for effective light-sheet microscopy. This problem was then addressed in 2014 by Hiroki Ueda and colleagues, who developed clear, unobstructed brain/body imaging cocktails and computational analysis (CUBIC), an efficient hydrophilic tissue-clearing method (Susaki et al., 2014). They used a systematic chemical screening strategy and found a series of amino alcohols, which can be used to delipidate and decolorize mammalian brains. CUBIC protocols for whole-body clearing also seem to permit light-sheet imaging of heart, lung, liver, kidney, pancreas, and other organs (Susaki et al., 2014, 2015; Tainaka et al., 2014), although whole-body imaging still has not been rigorously demonstrated because of the lack of an objective definition of whole-body imaging. One of the possible definitions for whole-body or -organ imaging would be the successful detection of cells or cellular nuclei in a whole body or a whole organ with more than a certain level of accuracy (e.g., 95% accuracy).

Further chemical screening and profiling led to the development of a series of CUBIC reagents (CUBIC-L or CUBIC-HL for delipidation, CUBIC-R+ for RI matching, CUBIC-B for decalcification of bone, CUBIC-P for decolorization, and CUBIC-X for tissue expansion) (Kubota et al., 2017; Murakami et al., 2018; Tainaka et al., 2018). Parallel efforts revealed the chemical principles of each tissue-clearing process (Susaki and Ueda, 2016; Tainaka et al., 2016, 2018). CUBIC-based clearing was extended to the fruit fly *D. melanogaster*. With this approach (FlyClear), endogenous fluorescence in whole undissected animals was preserved across developmental stages from larva to adult fly (Pende et al., 2018). In addition to these CUBIC-related reagents, other hydrophilic tissue-clearing reagents with different purposes have been independently developed, including thiodiethanol (TDE) immersion (Aoyagi et al., 2015; Costantini et al., 2015; Hasegawa et al., 2016; Staudt et al., 2007); see deep brain (SeeDB) (Ke et al., 2013); Sca*l*eS (sorbitol-based sca*l*e) (Hama et al., 2015); FRUIT (a cocktail of fructose and urea) (Hou et al., 2015); urea-based amino-sugar mixture (UBasM) (Chen et al., 2017); clearing-enhanced 3D (Ce3D) (Li et al., 2017); see deep brain 2 (SeeDB2) (Ke et al., 2016); $Clear^{T}$ (formamide) $/Clear^{T2}$ (a cocktail of formamide and polyethylene glycol) (Kuwajima et al., 2013); Warner's method (Warner et al., 2014); ClearSee (Kurihara et al., 2015); rapid clearing method based on triethanolamine and formamide (RTF) (Yu et al., 2018); illuminate cleared organs to identify target molecules (LUCID) (Mizutani et al., 2018); a series of sugars, sorbitol (Hirshburg et al., 2007) and sucrose (Chance et al., 1995; Tsai et al., 2009); and a series of X-ray contrast, Histodenz in refractive index matched solution (RIMS) protocol (Yang et al., 2014) and iodixanol in system-wide control of interaction time and kinetics of chemicals (SWITCH) protocol (Murray et al., 2015).

In parallel with the development of hydrophobic and hydrophilic tissue-clearing methods, a hydrogel-based tissue-clearing method called clear lipid-exchanged acrylamide-hybridized rigid imaging/immunostaining/in situ-hybridization-compatible tissue hydrogel (CLARITY) was also developed in 2013 by Karl Deisseroth and Kwanghun Chung. In this process, lipids are removed by perfusion of sodium dodecyl sulfate (SDS), a strong

detergent, and tissue is subsequently transformed into a clear acrylamide gel retaining biological elements (Chung et al., 2013). CLARITY employs an electrophoresis step to accelerate tissue clearing and is therefore more complex than many other hydrophobic and hydrophilic tissue-clearing methods that rely on passive diffusion. Following SDS perfusion, proteins and nucleic acids are retained, presumably because of their stabilization by the exogenous acrylamide gel. Using CLARITY, it may be possible to visualize endogenous fluorescent proteins and to label epitopes with fluorescent antibodies (Chung et al., 2013). Although reliable fluorescence preservation and immunolabeling remain challenging, intact CLARITY-processed brains have been successfully imaged at high resolution (numerical aperture [NA] = 1.0) with light-sheet microscopy (Tomer et al., 2014). Raju Tomer and colleagues developed the passive CLARITY technique (PACT) by decreasing gel density to improve tissue permeability and probe penetration (Tomer et al., 2014). Viviana Gradinaru and colleagues combined PACT with PARS (perfusion-assisted agent release *in situ*) to render rodent bodies transparent (Treweek et al., 2015; Yang et al., 2014). Other variations of CLARITY have been applied to bones (Greenbaum et al., 2017a) and for the detection of RNA (Greenbaum et al., 2017b; Yang et al., 2014). Sensitive methods for fluorescence *in situ* hybridization have been used to effectively visualize single RNA molecules within tissue (Shah et al., 2016).

Hydrogel-based methods have been further exploited to achieve super-resolution imaging. Expansion microscopy, developed by Ed Boyden and colleagues, uses a swellable hydrogel to isotropically expand tissues. Expanded structures within tissue may enable imaging at an effective resolution higher than that achievable using conventional microscopy (Chen et al., 2015). Kwanghun Chung and colleagues developed another hydrogel-based expansion microscopy method, magnified analysis of proteome (MAP), in which they omitted the protein digestion process to preserve proteins in the expanded brain (Ku et al., 2016), and recently introduced stabilization under harsh conditions via intramolecular epoxide linkages to prevent degradation (SHIELD), in which they used polyepoxy chemicals to protect florescence, antigenicity, transcripts, and tissue architecture (Park et al., 2018). Similar to hydrophobic and hydrophilic tissue-clearing methods, variations of hydrogel-based tissue-clearing reagents with different purposes have been developed, including optimized CLARITY (Lee et al., 2014), CLARITY-TDE (Costantini et al., 2015), plant-enzyme-assisted (PEA)-CLARITY (Palmer et al., 2015), simplified CLARITY (Lai et al., 2016), active clarity technique-pressure related efficient and stable transfer of macromolecules into organs (ACT-PREST) (Lee et al., 2016), and fast free-of-acrylamide clearing tissue (FACT) (Xu et al., 2017)

Since the earliest combined use of hydrophobic (Dodt et al., 2007), hydrophilic (Susaki et al., 2014), or hydrogel-based (Tomer et al., 2014) tissue-clearing methods and modernized light-sheet microscopy, the performance of tissue-clearing approaches and light-sheet microscopy has been continuously improved, broadening their utility (Ariel, 2017; Azaripour et al., 2016; Chakraborty et al., 2019; Fu et al., 2016; Gradinaru et al., 2018; Hörl et al., 2018; Migliori et al., 2018; Richardson and Lichtman, 2015; Silvestri et al., 2016; Susaki and Ueda, 2016; Tainaka et al., 2016; Voigt et al., 2019) (Figure 1). Indeed, with advanced tissue-labeling and -staining techniques, tissue-clearing methods, and light-sheet microscopy, whole-brain profiling of cells can be performed comprehensively and efficiently (Belle et al., 2014; Murakami et al., 2018; Renier et al., 2014, 2016; Susaki et al., 2014; Ye et al., 2016). Integration of tissue-clearing and light-sheet microscopy also promises to transform methods for interrogating the structure and connectivity of neural circuits spanning the brain (Ogawa and Watabe-Uchida, 2018; Economo et al., 2016, 2018; Winnubst et al., 2019).

The Present State of the Art and Challenges in Tissue Clearing

Tissue-clearing methods provide a powerful approach for optical imaging deep within biological specimens. Methods for tissue clearing are under active development so that they may be applied to larger samples and to improve their compatibility with an expanded set of techniques for labeling and visualizing structural and biochemical features of tissues. The physical and chemical principles that underlie tissue-clearing processes are also of great interest (Figure 2), and enhanced understanding of these processes continues to drive the development of new tissue-clearing methods.

Improvements in tissue-clearing methods have relied both on identification and application of more effective tissue-clearing chemicals (Pan et al., 2016; Tainaka et al., 2014, 2018) and on enhanced fixation procedures that permit the use of harsher reagents and procedures (e.g., strong detergents and high temperature) (Murray et al., 2015; Park et al., 2018; Yang et al., 2014). The identified potent tissue-clearing chemicals or conditions have been applied not only to entire bodies of rodents (Pan et al., 2016; Tainaka et al., 2014; Yang et al., 2014) but also to entire human organs, including a lymph node (Nojima et al., 2017), a kidney (Tainaka et al., 2018; Zhao et al., 2019), an eyeball, and even a human brain (Zhao et al., 2019).

Tissue-clearing methods, whether hydrophobic, hydrophilic, or hydrogel based, attempt to minimize light scattering—especially Mie scattering (Tuchin, 2015)—caused by mismatches in the RIs of different components of biological materials (e.g., lipids and proteins) with the RI of the medium (e.g., water) (Figure 2A, light scattering). Among biological materials, water usually exhibits the lowest RI (~1.33), dried lipids exhibit intermediate RIs (1.46–1.48) (Kienle et al., 2014; Pusterla et al., 2017), dried proteins and DNA exhibit higher RIs (1.540–1.598 for dried proteins, Bashkatov et al., 2018; ~1.58 for dried DNA, Inagaki et al., 1974), and hydroxyapatite (HAp) extracted from bone tissue exhibits the highest RI (1.600–1.604) (Antonio, 1949; Ascenzi and Fabry, 1959). In addition to reducing light scattering caused by inhomogeneity of RIs, tissue-clearing methods minimize light absorption caused by pigments such as heme (Figure 2A, light absorption).

Practically, most tissue-clearing methods aim to preserve proteins and/or nucleic acids while removing other components of tissue. Effective tissue-clearing methods usually achieve the following five chemical processes: (1) removing lipids (delipidation) and (2) removing HAp (decalcification) to reduce the inhomogeneity of RIs in biological samples; (3) removing pigments (decolorization) to reduce light absorption; (4) embedding in a hydrophobic solvent or aqueous medium with an RI matching

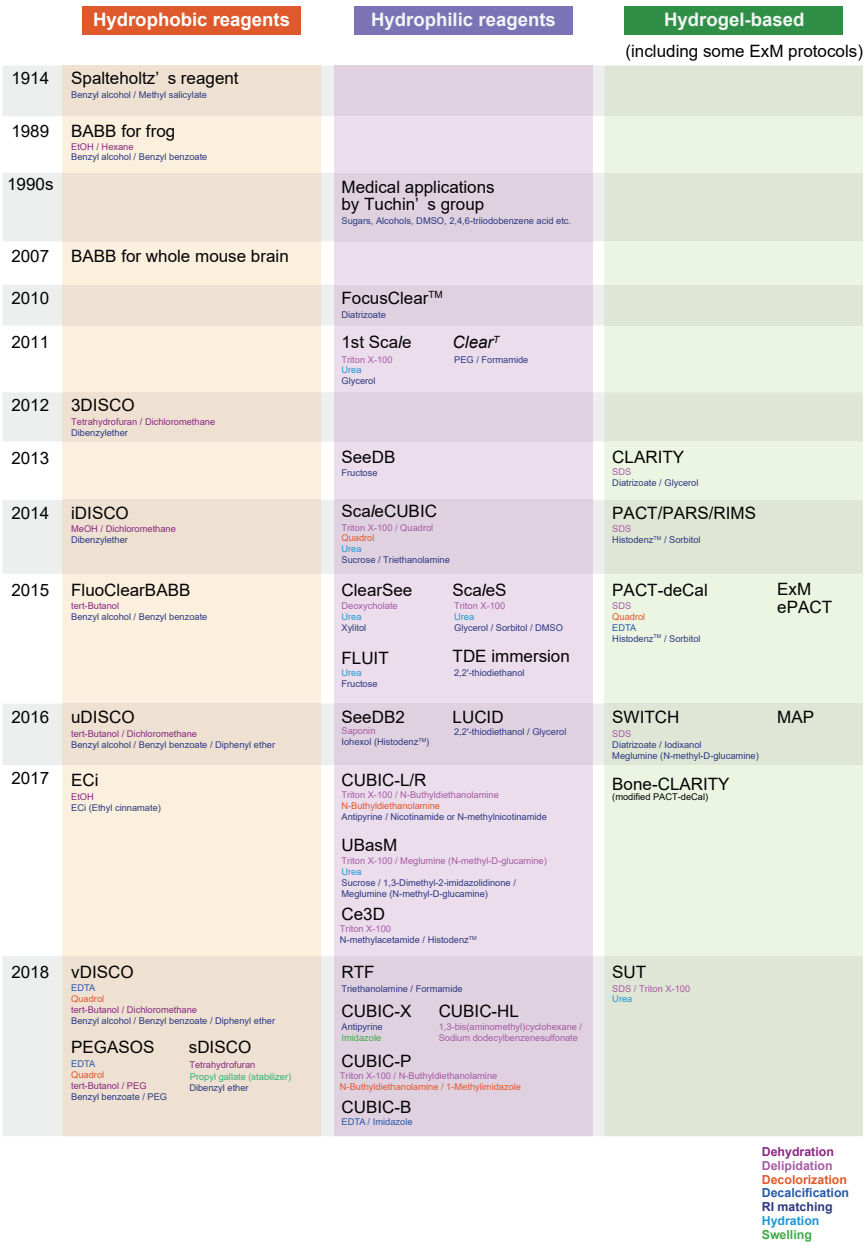

Figure 1. Timeline of Advances in Tissue-Clearing Methods

the remaining components of the tissue; and (5) sometimes expanding biological samples and thus contributing to RI matching (Figure 2B, RI matching). The RIs of RI-matching media differ across hydrophilic (1.52 for CUBIC-R+), hydrogel-based (1.45–1.49 for RIMS), and hydrophobic (1.56 for 3DISCO) methods, likely reflecting commensurate sample expansion and shrinkage (Kubota et al., 2017; Tainaka et al., 2016, 2018).

The optimal RIs of different tissue-clearing methods have been explained by considering a physical property of natural biological tissue (Murakami et al., 2018). As predicted from a pioneering study on cross-linked gels of extracted natural polymers such as DNA (polynucleotide), protein (polypeptide), and agarose (polysaccharide) by Amiya and Tanaka (1987), a recent study has revealed that fixed and delipidated natural organs behave as an electrolyte polymer gel even without exogenous polymers (Murakami et al., 2018). If a biological tissue acts as a polymer gel, the average RI (R_p) of the biological tissue (polymer gel) could be described by the average RI (R_m) and volume V_m of its components (monomer) according to the Lorentz-Lorenz equation (Figure 2C, light scattering) (Lorenz, 1880; Lorentz, 1880), where the average RI of biological tissue R_p is an increasing function of R_m/V_m. Therefore, the expansion and shrinkage of biological tissues lead to the decrease and increase of the average RIs, respectively, which should be matched by RI-matching media (Figure 2B, RI matching).

As described earlier, the average RI of biological tissues can be matched by an RI-matching medium. However, a remaining issue in delipidated, decalcificated, and decolorized biological samples (i.e., cross-linked gels of natural polymers such as proteins and nucleic acids) is the localized deviation of the RIs of these polymers from the average RI of the sample (and hence from the RI-matching medium). One possible solution to address this RI-deviation problem would be RI mixing to dissolve such light-scattering materials (i.e., materials of deviation of RIs from the average RI) into the RI-matching medium, because light scattering (Mie scattering) depends not only on RI mismatch but also on the size of the light-scattering materials (Figure 2B, RI mixing). If the effective size of the light-scattering materials (e.g., proteins with a micrometer-scale structure) could become sufficiently smaller than the wavelength of visible lights (0.38–0.75 μm) by dissolving them into the medium, the RIs of materials can be mixed with those of medium and/or other dissolved light-scattering materials nearby within the wavelength of visible lights. Hence, this RI-mixing process would effectively cancel out RI deviation of different light-scattering materials. Importantly, pursuits of RI-matching reagents have already identified a couple of chemicals that might have this RI-mixing property. For example, chemical screening of more than 1,600 hydrophilic chemicals identified effective RI-matching reagents (Tainaka et al., 2018), some of which (e.g., imidazole and antipyrine) also exhibit strong interaction with cross-linked natural polymers such as a gelatin gel (Murakami et al., 2018). Interestingly, known

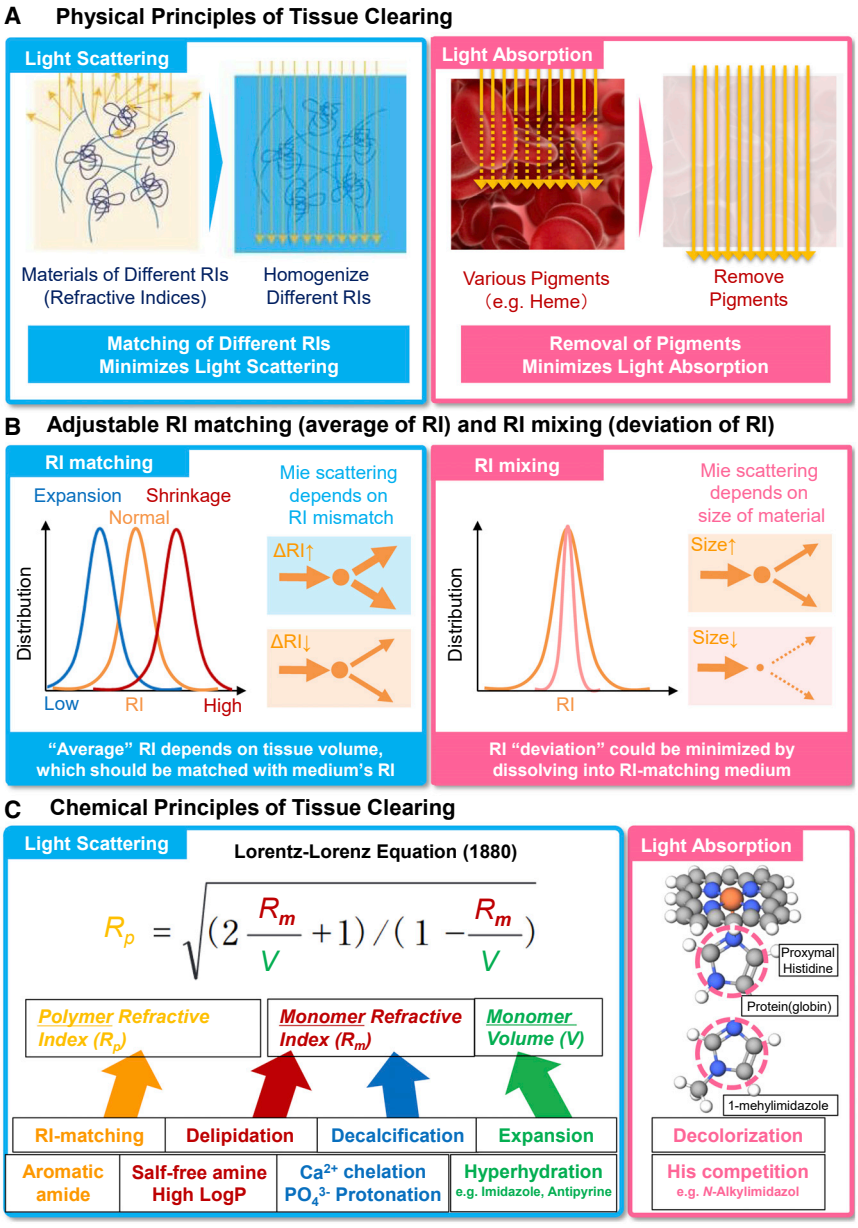

Figure 2. Physical and Chemical Principles of Tissue Clearing

(A) Classical physical principles of tissue clearing proposed in 1911 by Spalteholz. Light scattering can be minimized by homogenization of RIs of materials, whereas light absorption can be minimized by removing pigments.

(B) Adjustable RI matching (matching the tissue-size-dependent average RI of biological samples with RI-matching medium) and RI mixing (dissolving light-scattering materials into RI-matching medium to minimize RI deviation) proposed in this review. The average RI of biological samples depends on the size of tissues, which often expands in hydrophilic and hydrogel-based tissue-clearing methods, shrinks in hydrophobic tissue-clearing methods, and should be matched by RI-matching medium, because Mie scattering depends on the RI mismatch between those of light-scattering materials and medium. For the adjustable setpoint of average RI, see also the Lorentz-Lorenz equation in (C). The RI-deviation problem could be solved by RI mixing by dissolving light-scattering materials (i.e., materials of deviation of RIs from the average RI) into RI-matching medium, because light scattering or Mie scattering depends also on the size of the light-scattering materials.

(C) Chemical principles of tissue clearing. Delipidation, decalcification, and expansion processes contribute to the composite RI of biological samples (calculated by the Lorentz-Lorenz equation), which should be matched by RI-matching medium. Decolorization of heme can be achieved by competitive binding of 1-methylimidazole or other amines to iron-containing heme instead of histidine in globin. Each tissue-clearing chemical process is associated with the characteristic chemical nature of the tissue-clearing chemicals.

RI-matching reagents (e.g., DMSO) can interact strongly with cross-linked natural polymers even without water, implying that this RI-mixing concept might be applicable to hydrophobic reagents. A unified understanding of the physical properties of biological materials and chemical properties of RI-matching and RI-mixing reagents will lead to the efficient engineering of average and deviation of RIs (RI engineering) in biological tissues to achieve optimal transparency of larger samples. In addition, the RI-mixing concept built upon Mie scattering theory and our model of RI matching through the Lorentz-Lorenz equation, both of which are proposed in this review, might represent substantial conceptual advancements in the physical principles of tissue clearing since Spalteholz first proposed the RI-matching concept in 1911.

In addition to physical principles of RI matching and RI mixing in biological tissues, chemical understanding of other tissue-clearing processes such as delipidation, decolorization, and decalcification have advanced (Figure 2C, light scattering). Delipidation removes lipids to reduce the inhomogeneity of RIs in biological samples and allows other reagents to diffuse deep into biological samples. Therefore, delipidation has already become a common component of hydrophobic, hydrophilic, and hydrogel-based tissue-clearing methods. In hydrophobic tissue-clearing methods such as BABB, 3DISCO, uDISCO, iDISCO+, and sDISCO, polar solvents including THF (3DISCO) (Becker et al., 2012, 2014; Ertürk et al., 2012, 2014; Hahn et al., 2019) and alcohols such as ethanol (BABB) (Dent et al., 1989), tert-butanol (FluoBABB and uDISCO) (Pan et al., 2016; Schwarz et al., 2015), and methanol (iDISCO+) (Belle et al., 2014; Renier et al., 2014, 2016) are used as the first step to remove water and partially remove lipids from biological samples. As a second step, hexane (BABB) (Dent et al., 1989) and DCM (3DISCO, uDISCO, and iDISCO+) (Becker et al., 2012, 2014; Ertürk et al., 2012, 2014) are used to extensively remove lipids. In hydrophilic tissue-clearing methods, the nonionic detergent Triton X-100

(Sca*l*e and CUBIC-1) (Hama et al., 2011; Susaki et al., 2014; Susaki and Ueda, 2016) and amino alcohols, including Quadrol (CUBIC-1) (Susaki et al., 2014; Susaki and Ueda, 2016), triethanolamine (CUBIC-2) (Susaki et al., 2014; Susaki and Ueda, 2016), and N-butyldiethanolamine (CUBIC-L) (Kubota et al., 2017; Tainaka et al., 2018), are used as potent delipidation chemicals. In hydrogel-based tissue-clearing methods such as CLARITY and PACT, the ionic detergent SDS (Chung et al., 2013; Treweek et al., 2015; Yang et al., 2014) is mostly used for delipidation. Improved delipidation procedures have led to the development of more efficient tissue-clearing protocols. The ionic detergent sodium dodecylbenzenesulfonate (CUBIC-HL) (Tainaka et al., 2018), non-ionic detergent 3-[(3-cholamidopropyl)dimethylammonio]-1-propanesulfonate (CHAPS) (Zhao et al., 2019), aliphatic amines such as 1,3-bis(aminomethyl)cyclohexane (CUBIC-HL) (Tainaka et al., 2018), and hexanediol (Inoue et al., 2019; Tainaka et al., 2018) were shown to be effective reagents for delipidation of human tissue. Because there is a trade-off between the strength of tissue clearing, especially delipidation, and the preservation of molecular and cellular organization in tissues, we should carefully choose the stringency of tissue clearing according to the required transparency for the imaging of the samples.

Decolorization removes pigments to reduce light absorption in biological samples. Heme in red blood cells can be eluted by amino alcohols such as Quadrol in mild chemical conditions (Tainaka et al., 2014). The hypothesis for decolorization of heme was proposed such that a basic nitrogen in amino alcohols may competitively bind to iron-containing heme instead of histidine in globin (Figure 2C, light absorption) (Tainaka et al., 2014, 2016). This competitive binding hypothesis was strongly supported by the identification of a more potent decolorization compound, 1-methylimidazole, from more than 1,600 chemicals (Tainaka et al., 2018), which almost completely mimics the functional residue of histidine. In addition, SDS in CLARITY and PACT successfully decolorizes heme, likely as a result of the denaturation of the heme-hemoglobin holoenzyme by SDS (Epp et al., 2015; Lee et al., 2014; Treweek et al., 2015).

Decalcification removes calcium phosphate to reduce light scattering in biological samples containing bone. The inorganic bone mineral, HAp, was used for chemical screening of 1,600 reagents by measuring the optical density 600 (OD_{600}) of a chemically treated HAp suspension. In addition to EDTA, which has been known as a strong calcium chelator, potent decalcification-enhancing compounds were identified. Imidazole was found to facilitate EDTA-based decalcification, perhaps because of the protonation of phosphate ions (Tainaka et al., 2018). This enhanced decalcification may be the result of both chelation of calcium ions by EDTA and protonation of phosphate ions by imidazole (Tainaka et al., 2018).

In addition to the empirical findings of efficient tissue-clearing reagents and/or conditions, a more unified understanding of tissue-clearing chemistry has been gradually obtained by chemical profiling of potent reagents (Tainaka et al., 2014, 2018). In particular, the chemical profiling of more than 1,600 chemicals has been conducted for delipidation, decolorization, decalcification, tissue expansion, and RI matching (Murakami et al., 2018; Susaki and Ueda, 2016; Tainaka et al., 2016, 2018). Based on these screens, we have hypothesized that delipidation is enhanced by salt-free amines with high logP (octanol-water partition coefficient). Similarly, decolorization appears to be associated with competitive binding to iron-containing heme against histidine by *N*-alkylimidazole and decalcification as a result of chelation of Ca^{2+} by EDTA and protonating of PO_4^{2-} by an organic base. Tissue expansion is facilitated by hyperhydration and RI matching by electron enrichment of an RI-matching medium by an aromatic amide (Figure 2C, light scattering and light absorption) (Murakami et al., 2018; Tainaka et al., 2018). Altogether, our advancing understanding of the principles underlying tissue clearing provide a foundation for new approaches suitable for specific biological applications.

Another important challenge in tissue clearing is labeling of tissues with antibody. Since the 1980s, tissue clearing followed by whole-mount antibody staining was attempted for comprehensive imaging of whole organs and body, especially for nervous systems of insects and shrimp and the *Xenopus* embryo (Beltz and Kravitz, 1983; Bishop and O'Shea, 1982; Dent et al., 1989). Recently, tissue clearing and staining was applied to 3D observation of murine and human embryos (Belle et al., 2017; Hsueh et al., 2017; Renier et al., 2014), various animal organs and bodies (Cai et al., 2018; Chung et al., 2013; Coutu et al., 2018; Gleave et al., 2013; Hama et al., 2015; Hasegawa et al., 2019; Kubota et al., 2017; Kumar et al., 2010; Renier et al., 2016; Sillitoe and Hawkes, 2002; Susaki et al., 2014; Tainaka et al., 2014; Yang et al., 2014), and pathological samples of human tissues (Chung et al., 2013; Hildebrand et al., 2018; Lai et al., 2018; Liu et al., 2016; Nojima et al., 2017; Tanaka et al., 2017; Zhao et al., 2019). To improve the penetration speed of antibodies in a large tissue sample, several approaches have been adopted. First, stringent permeabilization by several methods has been attempted to increase the pore size of fixed specimens and hence enhance the penetration of antibodies. These methods include (1) delipidation (Chung et al., 2013; Duve et al., 1983; Hama et al., 2015; Lai et al., 2018; Susaki et al., 2014; Yang et al., 2014; Zhao et al., 2019); (2) dehydration (Belle et al., 2014; Dent et al., 1989; Duve et al., 1983; Gleave et al., 2013; Renier et al., 2014, 2016; Sillitoe and Hawkes, 2002; Zhao et al., 2019); (3) weaker fixation (Gleave et al., 2013); and (4) partial protein digestion with proteases (Gleave et al., 2013; Kumar et al., 2010; Sillitoe and Hawkes, 2002). Second, weakening non-specific interactions between antibodies and fixed tissues using chemicals such as urea (Hama et al., 2015) or SDS (Murray et al., 2015) has been also attempted to inhibit trapping of antibodies and hence accelerate the diffusion of antibodies deep into the tissues. Third, active transports by electrophoresis (Kim et al., 2015a; Lee et al., 2016; Wang et al., 2018) or pressurization such as trans-cardinal perfusion (Cai et al., 2018; Yang et al., 2014) were also tested on tissue samples to enhance the penetration of antibodies. Finally, increasing the amounts of antibodies by their iterative supplies (Chung et al., 2013; Lai et al., 2018) or reducing the size of antibodies by using nanobodies (Cai et al., 2019) was also effective to increase the penetration rate of antibodies. At present, these attempts to increase the penetration rate of antibody can successfully label relatively small and thin tissues, partially dissected tissues, or embryonic tissues with the lesser

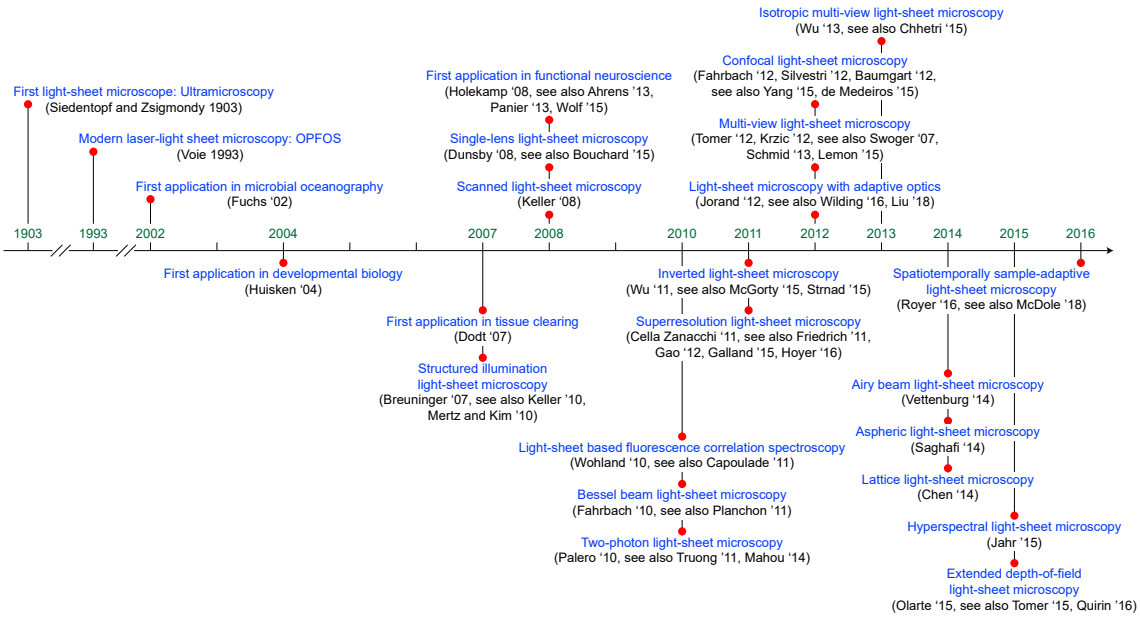

Figure 3. Timeline of Advances in Light-Sheet Microscopy

extracellular matrix. These attempts can also successfully stain an adult mouse brain or a dissected human specimen with relatively sparse epitopes such as c-Fos, amyloid plaques, or a microglia marker (Belle et al., 2014; Liebmann et al., 2016; Renier et al., 2014, 2016; Zhao et al., 2019). However, homogeneous antibody staining of adult mouse brains against high-density epitopes such as NeuN and neurofilament has not yet been adequately demonstrated and therefore remains a challenge in tissue clearing.

The Present State of the Art and Challenges in Light-Sheet Fluorescence Microscopy

Light-sheet fluorescence microscopy is a powerful technique for rapid and minimally phototoxic volumetric imaging of biological specimens. The high imaging speed, high signal-to-noise ratio, and high light efficiency of this method are the direct result of the central design principle in light-sheet imaging: a thin volume section of the specimen is selectively illuminated by a sheet of laser light, and fluorescence emitted from within this volume section is imaged onto a camera positioned at a right angle to the light sheet. The illuminated volume section and the detection focal plane are coplanar; thus, (1) no out-of-focus regions are exposed to laser light and (2) an image of the entire thin volume section can be acquired simultaneously. The first feature ensures that the specimen's photon budget is used efficiently and dramatically reduces photo-bleaching and photo-toxic effects compared with conventional and confocal fluorescence microscopy. The second feature provides high imaging speeds limited only by camera performance. This design facilitates rapid 3D imaging simply by moving the light sheet and detection focal plane through the specimen and acquiring a series of images across the volume. Because of these strengths, light-sheet microscopy has found widespread use throughout the life sciences over the course of the past decade and is employed routinely in the fields of developmental biology (Huisken et al., 2004; Keller et al., 2008; McDole et al., 2018; Rozbicki et al., 2015), cell biology (Chen et al., 2014; Liu et al., 2018; Nixon-Abell et al., 2016; Reichmann et al., 2018; Valm et al., 2017), and neuroscience (Ahrens et al., 2013; Chhetri et al., 2015; Dodt et al., 2007; Holekamp et al., 2008; Kawashima et al., 2016; Lemon et al., 2015; Panier et al., 2013; Wolf et al., 2015; Wan et al., 2019).

Although even the most basic implementations of light-sheet microscopy already offer key benefits, advances in microscope design have added strengths and synergies (Figure 3). These improvements have allowed microscopists to address many commonly encountered challenges in biomedical imaging, including fundamental limitations in spatial resolution, limitations in image quality arising from light scattering and aberrations, and limitations in the rapid imaging of large specimens.

Light scattering is a common problem in biological specimens with limited transparency, which includes most living, multicellular organisms. By introducing structured illumination (Breuninger et al., 2007; Keller et al., 2010) or line-confocal detection (Baumgart and Kubitscheck, 2012; de Medeiros et al., 2015; Fahrbach and Rohrbach, 2012; Silvestri et al., 2012) in light-sheet microscopy, the contribution of scattered light to image formation can be greatly reduced, thus improving contrast and resolution in deeper regions of the specimen. A complementary strategy for improving depth penetration (and reducing scattering in biological tissues) involves the use of longer-wavelength light for fluorescence excitation and relies on the principle of multi-photon excitation to allow a molecule to enter an excited state through concurrent absorption of multiple lower-energy photons. The use of this concept in light-sheet microscopy was first demonstrated for static light sheets (Palero et al., 2010) and then improved through integration in beam-scanning light-sheet microscopes (Mahou et al., 2014; Truong et al.,

2011). However, even with structured illumination, confocal detection, and multi-photon excitation, many biological specimens are too large to be imaged in high resolution in their entirety, primarily because of light scattering and absorption. To address this issue, light-sheet microscopy has been enhanced by multi-view imaging capabilities (Krzic et al., 2012; Lemon et al., 2015; Pende et al., 2018; Schmid et al., 2013; Swoger et al., 2007; Tomer et al., 2012). In such implementations, the specimen is illuminated by more than one light sheet (typically two light sheets from opposite directions) (Huisken and Stainier, 2007) and imaged by more than one camera (typically two cameras from opposing views), which improves physical coverage of large specimens without compromising temporal resolution or temporal continuity across the volume. Finally, scaling up light-sheet imaging to very large transparent specimens is feasible through the use of modified objective arrangements, as well as tiling strategies, in which sample translation can help overcome the limited field of view of the camera, and detection optics (Hörl et al., 2018; Migliori et al., 2018; Voigt et al., 2019).

Improvements in spatial resolution have become possible by using beam shaping to create thinner light sheets (Chen et al., 2014; Fahrbach and Rohrbach, 2010; Pende et al., 2018; Planchon et al., 2011; Saghafi et al., 2014; Sheppard, 2013; Vettenburg et al., 2014), as well as by using orthogonal multi-view imaging (Chhetri et al., 2015; Wu et al., 2013). In conventional light-sheet microscopes, axial resolution is typically substantially lower than lateral resolution—often by up to a factor of 5–10 when imaging a large field of view. Because axial resolution in the detection system can only be increased up to a limit imposed by the numerical aperture of the detection objective, one option for improving overall system resolution is the reduction of light-sheet thickness. Light sheets constructed from Bessel beams and optical lattices (Chen et al., 2014; Fahrbach and Rohrbach, 2010; Planchon et al., 2011) can be made thin enough to improve overall axial resolution to around 300–400 nm, which is comparable to the lateral resolution limit. However, the field of view of such microscopes is typically limited to around 100 μm along the illumination axis; thus, other solutions are needed for rapid, high-resolution imaging of larger specimens. By acquiring orthogonal views of a sample, followed by registration and multi-view deconvolution of these multiple views, images with near-isotropic spatial resolution on the order of 300–400 nm can be obtained without the need for constructing thin light sheets (and thus without the need to limit imaging to a small field of view) (Chhetri et al., 2015; Wu et al., 2013). In addition, complementary efforts are under way to investigate the design of light sheets that maintain a narrow beam waist over long spatial distances (Pende et al., 2018; Saghafi et al., 2014). Alternatively, the relationship between size of field of view and light-sheet-waist thickness can be decoupled by tiling or scanning the light-sheet waist across the field of view (Dean et al., 2015; Fu et al., 2016) or translating the sample relative to the light-sheet waist (Migliori et al., 2018), which provides more uniform illumination across the field of view.

Although the techniques described earlier offer high system resolution, the effective spatial resolution in a real biological sample can be substantially lower as a result of optical aberrations. Unfortunately, most biological specimens, even those that are relatively transparent, introduce significant aberrations that alter the path and shape of the light sheet and distort the shape of the detection focal plane. When limiting the observation to sufficiently small regions in the sample, thus ensuring that wavefront errors are relatively uniform across the small field of view, light-sheet microscopy can be combined with adaptive optics to efficiently compensate for most, if not all, of these distortions (Jorand et al., 2012; Liu et al., 2018; Wilding et al., 2016). However, conventional adaptive optics are typically unsuited to light-sheet applications that require rapid live imaging of large, optically heterogeneous specimens with a field of view exceeding 100 μm. In this latter scenario, geometrical mismatches between light sheets and detection focal planes can be rapidly mapped across the specimen (and over time) by real-time image processing and approximately corrected for through optical defocus and light-sheet tip and tilt manipulations (McDole et al., 2018; Royer et al., 2016). With this complementary approach, diffraction-limited performance of the light-sheet microscope can be at least partially recovered in specimens as large and complex as zebrafish, fruit fly, or mouse embryos, which typically provides a 2- to 5-fold improvement in spatial resolution.

Temporal resolution in light-sheet microscopy is generally limited by camera speed. To preserve the high frame rates offered, for example, by state-of-the-art scientific complementary metal–oxide–semiconductor (sCMOS) cameras in a volumetric imaging setting, the microscope's detection objective can be moved in synchrony with the light sheet by fast piezo positioners (Ahrens et al., 2013; Lemon et al., 2015). For example, high-performance piezos are capable of moving detection objectives at rates of several tens to hundreds of hertz for travel ranges of up to several hundred micrometers (Greer and Holy, 2019; Piezosystems_Jena, 2019; Wan et al., 2019). The advantage of this approach is that it ensures optimal image quality by always acquiring images at the native focal plane of the objective; however, the cost of a good piezo is not insignificant. Less expensive alternative solutions include the use of remote focusing with electric tunable lenses (Fahrbach et al., 2013) or extended depth-of-field detection (Olarte et al., 2015; Quirin et al., 2016; Tomer et al., 2015). The reduced cost and ability to keep the objective stationary come at the expense of a reduction in resolution and image quality, which result from imaging away from the native focal plane and, in the latter case, from the use of an elongated detection point-spread function.

Research in recent years has also produced a range of useful, alternative designs of light-sheet microscopy, such as implementations that are compatible with biological preparations on coverslips and other horizontal surfaces (McGorty et al., 2015; Strnad et al., 2016; Wu et al., 2011) or designs that use a single objective for illumination and detection (Bouchard et al., 2015; Dunsby, 2008). The latter concept sacrifices some optical performance by reducing the effective numerical aperture and acquiring images away from the native focal plane, but it also enables light-sheet imaging of samples with limited optical access and supports applications that constrain the placement and orientation of microscope optics.

Whole-Brain Profiling of Cells

Developments in microscopy have helped to bring about a method-driven renaissance in neuroanatomy that is distinguished

by a focus on large-scale projects generating unprecedented amounts of anatomical data. Quantitative, whole-brain profiling of the spatial distribution of cells, their molecular features, and their connectivity represents a powerful application of modernized tissue-clearing and light-sheet microscopy in neuroscience. Comprehensively mapping the distributions of neuronal and glial types across the brain allows brain regions to be delineated with unprecedented precision and their components to be defined, leading to an enhanced understanding of brain structure and facilitating comparisons across individuals and across species.

Until recent advances in genetic labeling, tissue processing, and light microscopy, comprehensively mapping cells throughout the brain has only been possible in simple organisms, such as the nematode *Caenorhabditis elegans* (White et al., 1986). The size and complexity of the mammalian brain present barriers to progress in understanding the organization of the nervous system of higher organisms. Accordingly, the classical anatomical literature of the mammalian brain has been piecemeal, with a given study typically examining only one or a few brain regions and one or a few cell types at a time, typically in the male brain. For example, the use of classical stereological methods has led to quantification of interneuron distribution in sensory cortices (Gonchar et al., 2008; Pfeffer et al., 2013; Prönneke et al., 2015; Rudy et al., 2011; Xu et al., 2010), but this approach has proven to be too laborious to be applied to whole-brain cell-type analyses (Glaser and Glaser, 2000; Schmitz and Hof, 2005; Williams and Rakic, 1988). A simple method, called isotropic fractionator, was developed for counting cell nuclei in suspension by flow cytometry after tissue dissociation and was successfully applied to comparative studies of neuronal and glial cell counts in the mouse brain and across a range of species (Herculano-Houzel et al., 2015a, 2015b, 2013; Kverková et al., 2018; Marhounová et al., 2019; Olkowicz et al., 2016). However, because the mammalian brain comprises many brain areas (e.g., mouse brain has >400 unique areas) that would need to be precisely dissected, this method is not appropriate for comprehensive analyses or easily adaptable for analysis of specific cell types.

Automated block-face imaging methods combining top-view light microscopy and integrated tissue sectioning enable high-quality, high-resolution brain-wide imaging. This approach substantially improved upon histological methods in which thin tissue sections are manually cut, mounted on slides, and imaged individually. The enhanced throughput of automated block-face imaging represents a critical factor for large-scale neuroanatomical projects. Imaging in a block-face configuration also provides enhanced reliability and minimal distortion, producing complete datasets that may be registered to standardized anatomical reference atlases—critical for integrating anatomical data from multiple experiments. Several block-face imaging methods have been developed. Serial two-photon tomography (STPT) takes advantage of two-photon excitation to provide optical sectioning in standard paraformaldehyde-fixed tissues. STPT can be used to generate a series of two-dimensional images spanning all regions of the brain (Kim et al., 2017; Osten and Margrie, 2013; Ragan et al., 2012) or full 3D image volumes spanning the brain (Economo et al., 2016). Knife-edge scanning microscopy (KESM) (Mayerich et al., 2008) and micro-optical sectioning tomography (fluorescence micro-optical sectioning tomography [fMOST]) (Gong et al., 2016; Li et al., 2010; Zheng et al., 2013) can also generate complete, 3D whole-brain imagine volumes using micron-scale sectioning and single-photon imaging of resin-embedded tissue. Block-face serial microscopy tomography (FAST) (Seiriki et al., 2017) uses a spinning-disk confocal microscope to achieve high imaging rates in a block-face configuration.

One application of these methods is brain-wide mapping of genetically defined cell types. For example, Osten and colleagues developed an automated, quantitative brain-wide cell profiling platform (qBrain) that can be used to map the brain-wide distribution of genetically defined cell types across regions in the mouse brain. qBrain combines recombinase-based knockin driver mouse lines that label genetically defined cell types (Huang, 2014; Huang and Zeng, 2013; Madisen et al., 2012), automated brain imaging at single-cell resolution by STPT, and computational analyses that include cell detection by convolutional neural networks (Kim et al., 2015b, 2017; Ragan et al., 2012). The application of this platform to cell-type anatomy has immediately demonstrated the power of unbiased, whole-brain anatomical mapping in uncovering novel principles of mammalian brain organization. First a comparison of quantitative distribution of three major inhibitory neuron cell types, those expressing somatostatin (SST), parvalbumin (PV), and vasoactive intestinal peptide (VIP), across the mouse brain isocortex revealed hierarchical organization of the neocortex, because sensory-motor areas were found to be dominated by output-modulating PV-positive interneurons, whereas association areas were composed of large numbers of input-modulating SST-positive interneurons. Another perhaps even more surprising finding from this study was the identification of nine brain regions with different distributions of these cell types between male and female mouse brains, with eight regions containing more VIP+ or SST+ neurons in the female brain despite the female brain being smaller overall than the male brain. Most regions with sexually dimorphic cell-type distributions were from the structures of the vomeronasal system, which regulate reproductive and social behaviors. This finding provides direct, quantitative evidence that anatomical differences underlie sexually dimorphic behaviors (Bayless and Shah, 2016; Simerly, 2002). Given the unexpected results derived from analyses of only 3 cell types using STPT, it seems likely that further quantitative atlasing of cell-type distributions will provide additional insights into how the cellular composition of different brain areas may contribute to their functions.

Block-face imaging methods remain attractive because of their high resolution and compatibility with large tissue samples. However, due to many of the technological advances reviewed here, large-volume imaging using tissue clearing and light-sheet microscopy are closing the gap and provide several key advantages over block-face methods. Block-face imaging requires specialized instruments that may not be readily accessible to many researchers, while light-sheet microscopes are becoming increasingly common fixtures in microscope facilities. Furthermore, light-sheet imaging can achieve acquisition rates for volumetric data that are several orders of magnitude faster than block-face imaging methods. Still, to realize whole-organ cell profiling, clearing methods must achieve high transparency of

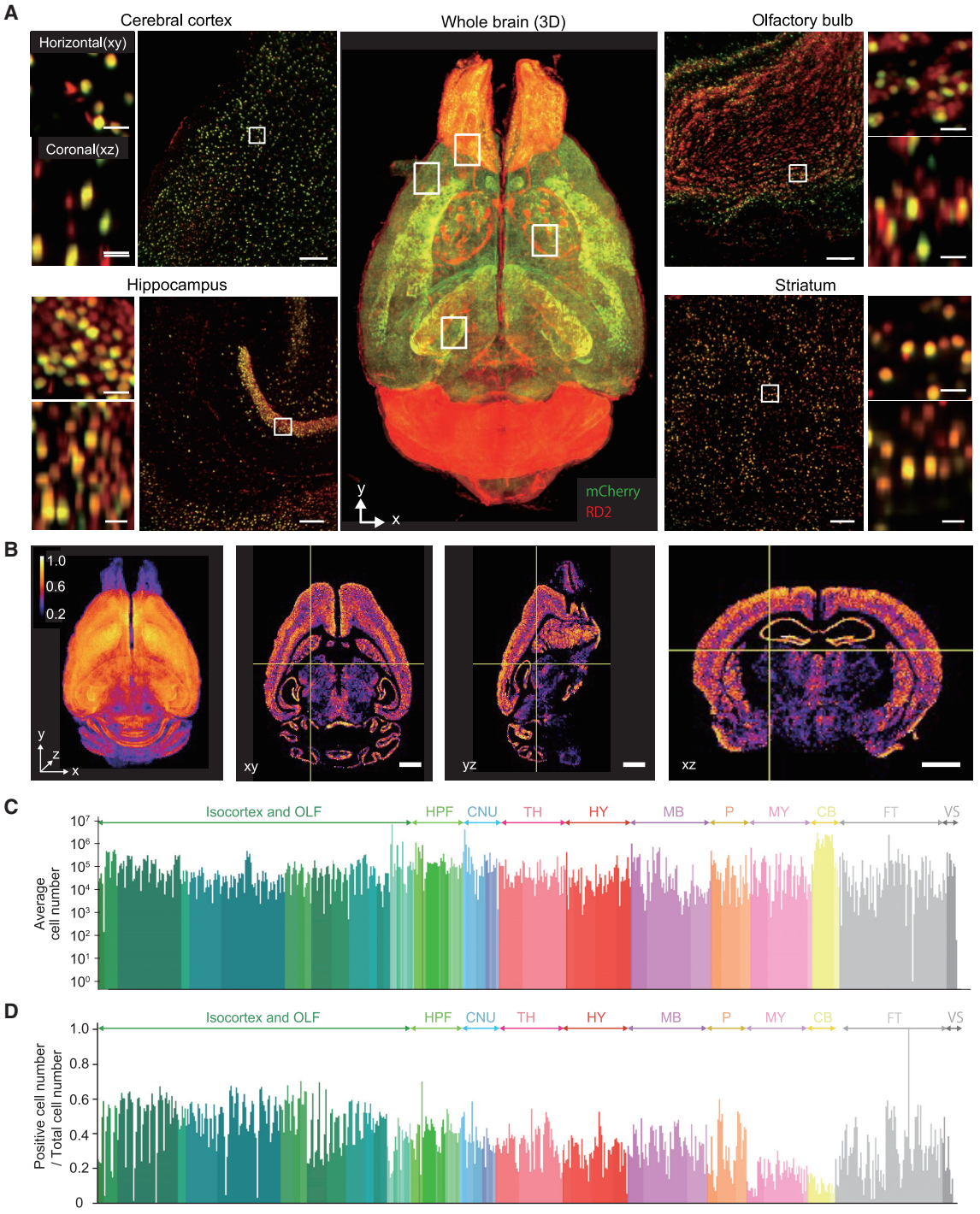

Figure 4. Whole-Brain Profiling of Cells by Light-Sheet Fluorescent Microscopy

(A) Volume-rendered and single-plane images of a brain transduced with AAV-PHP.eB:NSE-H2B-mCherry (mCherry, green) and counterstained by RD2 (red), which is cleared by CUBIC-L/R+. Overlapped signals are shown in yellow. A volume-rendered image is shown in the center. Single-plane and magnified images are shown for cerebral cortex, hippocampus, olfactory bulb, and striatum. Both horizontal (x-y) and coronal (x-z) views are also shown. Scale bars, 200 μm (single-plane image) and 25 μm (magnified image).

(B) 3D and cross-section images of the positive-cell-number ratio map of whole mouse brain infected by AAV-PHP.eB (NSE-H2B-mCherry). Voxel size, 80 μm. Scale bars, 2 mm and 50 μm.

(legend continued on next page)

samples so that the light sheet is not degraded by tissue-induced scattering, aberration, and absorption. In addition, light-sheet imaging methods must maintain consistent quality across large fields of view. Increasingly, these constraints can be met by state-of-the-art tissue-clearing methods and light-sheet fluorescent microscopy. As a result, this approach is becoming an appealing strategy for whole-brain profiling of cells in intact mammalian brains (Liebmann et al., 2016; Murakami et al., 2018; Renier et al., 2014, 2016; Susaki et al., 2014, 2015; Sylwestrak et al., 2016; Tatsuki et al., 2016; Tomer et al., 2014). For example, a tissue-clearing and expansion method, CUBIC-X, in combination with custom-made light-sheet fluorescent microscopy with a 10× objective lens (NA = 0.6, working distance = 8 mm), allowed 1.3 million images covering the entire mouse brain to be successfully obtained.

Whole-brain datasets generated by these instruments range from ~100 GB to ~30 TB of data per single mouse brain, necessitating the development of new computational tools for analyses. 3D reconstructions, anatomical registration, and signal detection and quantification, for example, have been demonstrated using supervised machine learning algorithms trained on expert-annotated ground truth data (Hawrylycz et al., 2011; Kim et al., 2015b; Kuan et al., 2015; Ng et al., 2007; Ragan et al., 2012). In datasets collected using CUBIC-X, GPU-based image analysis was used to extract the 3D coordinates of all cells in the adult mouse brain. Leveraging existing anatomical segmentations of the mouse brain (Dong, 2008; Lein et al., 2007), this approach yielded a whole-brain atlas with single-cell resolution (CUBIC-Atlas) (Murakami et al., 2018). Further development of the cell detection algorithm improved the accuracy and speed of this analysis pipeline so that more than 90% of cells in the mouse brain could be identified in several hours (up to 2 TB/h) (Matsumoto et al., 2019). Using this cell-nucleus detection algorithm, the updated CUBIC-Atlas 1.2 of 8-week-old C57BL/6J mouse brain was constructed that contains the spatial coordinates and brain regions associated with more than 10^8 cells (Matsumoto et al., 2019). The improved throughput offered by these protocols allows the analysis of numerous (>100) samples, providing a highly versatile platform for biomedical research, including comparative analyses across a range of mammalian and vertebrate species, and opening a new and exciting frontier in neuroanatomy (Figure 4).

The molecular features of cells in the brain—their transcriptomes and proteomes—provide information extending beyond their morphology—both about their type and about the cellular processes related to function. Classic approaches for immunofluorescence and fluorescence *in situ* hybridization for labeling proteins and mRNAs, respectively, have been most frequently applied within thin tissue sections through which fluorophore-conjugated macromolecules can quickly diffuse. In addition to reducing the scattering and absorption of light, processes such as delipidation and hydrogel embedding increase the diffusivity of proteins and oligonucleotides within tissue. Therefore, there is a natural synergy between techniques for clearing tissue samples and for labeling the mRNAs and proteins within them. Nevertheless, devising methods that permit the penetration of antibodies (for immunofluorescence) and oligonucleotides (for *in situ* hybridization) into tissue samples as large as intact organs has remained challenging. Penetration of macromolecules into tissues cleared using various clearing techniques has been demonstrated, for example, by CLARITY (Chung et al., 2013), iDISCO+ (Renier et al., 2016), vDISCO (Cai et al., 2018), CUBIC-L/R+, and CUBIC-X (Matsumoto et al., 2019; Murakami et al., 2018). Nevertheless, uniformly staining thick samples—particularly intact, adult mammalian brains—may require protocol and/or probe optimization to effectively label different molecular targets. In addition, molecular labeling may be time consuming, requiring several weeks or months for probes to thoroughly penetrate large samples even following delipidation and/or hydrogel embedding. Active processes, such as stochastic electrotransport, may accelerate macromolecule diffusion (Kim et al., 2015a; Lee et al., 2016). Ongoing methodological development aims to increase the speed, reliability, and set of molecular targets that may be labeled in cleared tissue.

One powerful application of whole-brain tissue clearing and molecular labeling is efficient, brain-wide identification of cells expressing immediate early genes (IEGs). The expression of IEGs such as c-*fos*, *Arc*, *Egr-1*, *FosB*, and *Npas4* marks transcriptionally activated neurons and that can be used as an indirect measure of cells that have been recently active. Whole-brain mapping of IEG-expressing neurons using tissue clearing and light-sheet imaging has been demonstrated using iDisco+ (Renier et al., 2016) to delineate the brain-wide set of neural circuits engaged by parenting behavior. Identifying neural circuits using this approach allows the neural circuits engaged by neural processes to be mapped efficiently and comprehensively across the brain.

Whole-Brain Profiling of Circuits

The recent proliferation of neuroanatomical methods has also enabled whole-brain profiling of connectivity in the brain. Connectivity determines how information flows through neural circuits, giving rise to the diversity of mammalian behaviors from the simple startle response of defensive behaviors to the complex neuronal computations during cognitive and emotive processing. Mesoscale connectivity, which describes the long-range projections of neural populations, controls which brain areas are connected (Mitra, 2014). At the microscale, mapping the brain-wide connectivity of single neurons provides a fine-scale description of how signals are routed between brain areas. Mapping connectivity using light microscopy at both the mesoscale and the microscale involves more stringent requirements for resolution and contrast than mapping cells,

(C) Average cell number of all anatomical regions in three 8-week-old C57BL/6N mouse brains. Only the edge regions (i.e., having no child region) are shown. OLF, olfactory areas; HPF, hippocampal formation; CNU, cerebral nuclei; HY, hypothalamus; MB, midbrain; P, pons; MY, medulla; CB, cerebellum; FT, fiber tract; VS, ventricular system.
(D) Positive-cell-number ratio of each anatomical region in mouse brain infected by AAV-PHP.eB (NSE-H2B-mCherry). The data and figure are adopted from Matsumoto et al. (2019).

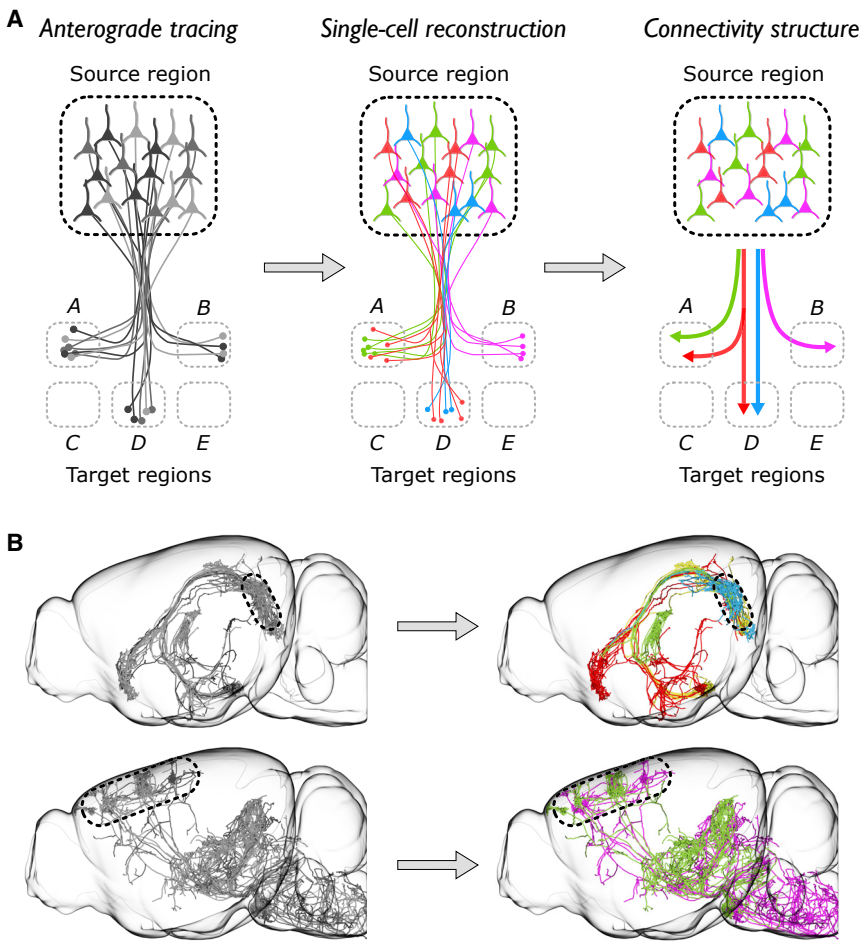

Figure 5. Whole-Brain Profiling of Circuits

Single-neuron reconstruction reveals structured connectivity patterns.

(A) Left, anterograde tracing of a population of neurons in a source brain region can reveal regions of the brain to which the source connects (i.e., regions A, B, and D, but not C and E). Middle, single-cell axonal reconstruction reveals where individual neurons connect. Right, from single-neuron reconstructions, classes of neurons with similar connectivity can be identified and structured patterns of connectivity across a population can be determined.

(B) Top left, single-neuron reconstructions of projection neurons in the subiculum (boxed region). Top right, axonal reconstructions reveal distinct brain-wide patterns of connectivity (color coded) (Cembrowski et al., 2018; Winnubst et al., 2019). Bottom left, single-neuron reconstructions of pyramidal tract neurons in the motor cortex (boxed region). Bottom right, axonal reconstructions reveal two distinct types of pyramidal tract neurons based on their brain-wide connectivity (green, magenta) (Economo et al., 2018).

because axonal processes with diameters much smaller than neuronal somata must be detected with high fidelity. Therefore, block-face imaging methods have remained the dominant approach and have been deployed successfully for mapping connectivity. At the mesoscale, STPT has been used to map the long-range connectivity of thalamic projections, connections between the cortex and the striatum, and perhaps most notably, region-to-region connectivity as part of the Allen Institute for Brain Science Mouse Connectivity Project. This project has assayed the brain-wide projections of genetically identified populations of cells in hundreds of brain regions (Oh et al., 2014).

Although mapping mesoscale connectivity effectively identifies the set of brain regions to which a neural population projects, microscale connectivity controls how those connections are structured at the cellular level. This information is crucial for identifying cell types and defining how information is represented and communicated between brain areas (Figure 5). To determine long-range connectivity in the brain with single-neuron resolution, Economo and colleagues extended STPT to full, volumetric imaging of the mouse brain by increasing the acquisition rate by 20-fold and combining it with tissue clearing (Economo et al., 2016) and sparse neuronal labeling. In doing so, they were able to reconstruct the axonal projections of single neurons in their entirety. Using whole-brain imaging to determine axonal connectivity increased the efficiency of this process by several orders of magnitude compared with existing histological approaches (Economo et al., 2019). Efficient, single-neuron reconstruction has also been demonstrated using fMOST (Li et al., 2018). These methods have enabled the brain-wide projections of more than 1,000 neurons to be reconstructed in their entirety (Winnubst et al., 2019). Mapping connectivity at the microscale has been instrumental for revealing the heterogeneity of projection neurons and the structure of the projection pathways they comprise in motor (Economo et al., 2018), somatosensory (Hooks et al., 2018), and visual (Han et al., 2018) cortices; hippocampus (Cembrowski et al., 2018); and claustrum (Wang et al., 2019). Despite the success of projects using block-face imaging to map long-range connectivity in the brain, instruments designed for this purpose are not widely available to most researchers. Advances in light-sheet microscopy (Chhetri et al., 2015; Keller and Dodt, 2012; Verveer et al., 2007) promise to substantially reduce the time necessary for brain-wide imaging with sufficient resolution to resolve and reconstruct axons, increasing the efficiency of this process and enabling comprehensive atlasing of long-range connectivity patterns in the mammalian brain (Economo et al., 2019).

Future Perspective

Seamless integration of tissue-clearing methods and light-sheet microscopy will continue to enable key applications in neuroscience, including whole-brain profiling of cells and circuits in rodents. In the near future, improvement of clearing, staining, imaging, and image informatics will expand the spectrum of applications to whole-brain profiling of cells in primates and humans, one of the grand challenges in neuroscience. Isotropic imaging of

cleared and 5-fold expanded entire mouse brains at 1.3 × 1.3 × 1.3 μm resolution gives rise to ~2.5 TB of data per brain (~0.5 TB × 5-fold volume expansion) and is estimated to be sufficient for extracting cell-nucleus information and constructing 3D single-cell-resolution whole-brain atlases. Because marmoset brains (~7.6 g) and human brains (~1,330 g) are approximately 15- and 2,660-fold larger, respectively, than mouse brains (~0.5 g) (Stephan et al., 1981), whole-brain profiling of marmoset and human brains will give rise to ~38 TB and 6.65 PB of data, respectively, and provide single-cell-resolution whole-brain atlases comprising ~1.5 × 10^9 and ~2.7 × 10^{11} cells, respectively. To achieve whole-brain profiling of cells in primates and humans, several remaining issues need to be addressed. One of the remaining issues toward this goal is more stringent delipidation. Although the chemistry of the delipidation process in tissue clearing has been greatly advanced by chemical screening and profiling (Inoue et al., 2019; Tainaka et al., 2018; Zhao et al., 2019) and by developing stringent fixation protocols (Park et al., 2018), delipidation of the lipid-rich brains of marmosets and humans may require improvements in delipidation chemistry, in particular for the white matter of the brain. Another remaining issue is auto-fluorescence, in particular human brain specimens. Because the human brain is usually fixed in formaldehyde for a long period, there is a need for minimizing auto-fluorescence arising from long-term fixation. The third issue on the path toward whole-brain profiling of cells in such large brains is the need for development of optimal microscopy for marmoset and human brains. Because a marmoset brain is 15 times larger than a mouse brain, the development of new, large-aperture optics with the long working distance required to cover the entire marmoset brain will be necessary. As far as human brains are concerned, an imaging strategy based on physical sectioning of the brain will likely present the most promising approach. Even in this case, advancements in microscopy will be essential for rapid, high-resolution imaging of the resulting thick slices (e.g., ~5 mm thickness) with a cross-section area of ~100 cm^2. Especially for such large tissue samples that may even comprise human tumors (Dodt et al., 2015), light sheets with an extended Rayleigh range (Saghafi et al., 2014) could be particularly helpful. In addition, more powerful image informatics are needed to accurately and rapidly extract information from terabyte- and petabyte-scale datasets. Although these challenges may seem daunting at present, we believe that they will likely be solved in the near future, enabling the construction of 3D single-cell-resolution whole-brain atlases that serve as a foundation upon which to integrate additional information, such as cell types, cell states (e.g., c-Fos expression), and cellular connectivity.

In the realm of structural connectivity, whole-brain profiling of circuits at the single-neuron level presents another grand challenge for mammalian neuroscience. As discussed earlier, a recent study characterized the long-range axonal projections of more than 1,000 neurons from a few key areas in the mouse brain (Winnubst et al., 2019). However, a detailed brain-wide classification of neurons into morphological cell types in the mouse brain would likely require a sampling of at least 100,000 neurons (~0.1% of all cells in the mouse brain, because it is estimated that there are ~1,000 brain regions in the mouse brain and likely more than 10 cell types per region) (Winnubst et al., 2019). Furthermore, a more complete description of neuronal cell types would require establishing correspondences of morphology, gene expression, and function at the single-neuron level. Faster imaging afforded by novel light-sheet approaches, together with increased throughput in the reconstruction process (a 10- to 20-fold improvement over the current state of the art) because of further automation, could make this goal achievable in a few years. Obtaining such comprehensive information on the structural organization of the brain will provide foundational information necessary for functional insights into the mammalian brain in health and disease.

ACKNOWLEDGMENTS

We thank E.A. Susaki for helping to construct Figure 1 for advanced tissue-clearing methods, K. Matsumoto for helping to construct Figure 4 and Johan Winnubst for help with renderings in Figure 5. We also gratefully acknowledge grant support from Brain/MINDS JP20dm0207049, Science and Technology Platform Program for Advanced Biological Medicine JP20am0401011, AMED-CREST JP20gm0610006 (AMED/MEXT) (to H.R.U.), Grant-in-Aid for Scientific Research (S) JP25221004 (JSPS KAKENHI) (to H.R.U.), and HFSP Research Grant Program (HFSP RGP0019/2018) (to H.R.U.) as well as funding from the Austrian Science Fund (FWF) and the Vienna Science Fund (WWTF) (to H.-U.D.), the Howard Hughes Medical Institute (to P.J.K., M.N.E., and J.C.), and NIMH U01 MH105971 and U01 MH114824 (to P.O.).

AUTHOR CONTRIBUTIONS

H.R.U., H.-U.D., and P.J.K. wrote the introduction section; H.R.U. wrote the tissue-clearing section; P.J.K. and H.-U.D. wrote the light-sheet microscopy section; P.O., M.N.E., and H.R.U. wrote the whole-brain cell profiling section; M.N.E. and J.C. wrote the whole-brain circuit profiling section; and H.R.U. and P.J.K. wrote the future perspective section. All authors discussed and commented on the manuscript text.

DECLARATION OF INTERESTS

H.R.U. is a co-inventor on patent applications covering the CUBIC reagents and a cofounder of CUBICStars Inc. P.J.K. is a co-inventor on patents and patent applications covering multi-view and adaptive light-sheet microscopy. P.O. is a cofounder of Certerra Inc. and Certego Therapeutics Inc.

REFERENCES

Ahrens, M.B., Orger, M.B., Robson, D.N., Li, J.M., and Keller, P.J. (2013). Whole-brain functional imaging at cellular resolution using light-sheet microscopy. Nat. Methods *10*, 413–420.

Amiya, T., and Tanaka, T. (1987). Phase transitions in crosslinked gels of natural polymers. Macromolecules *20*, 1162–1164.

Antonio, A. (1949). Quantitative researches on the optical properties of human bone. Nature *163*, 604.

Aoyagi, Y., Kawakami, R., Osanai, H., Hibi, T., and Nemoto, T. (2015). A rapid optical clearing protocol using 2,2′-thiodiethanol for microscopic observation of fixed mouse brain. PLoS ONE *10*, e0116280.

Ariel, P. (2017). A beginner's guide to tissue clearing. Int. J. Biochem. Cell Biol. *84*, 35–39.

Ascenzi, A., and Fabry, C. (1959). Technique for dissection and measurement of refractive index of osteones. J. Biophys. Biochem. Cytol. *6*, 139–142.

Azaripour, A., Lagerweij, T., Scharfbillig, C., Jadczak, A.E., Willershausen, B., and Van Noorden, C.J. (2016). A survey of clearing techniques for 3D imaging of tissues with special reference to connective tissue. Prog. Histochem. Cytochem. *51*, 9–23.

Bashkatov, A.N., Berezin, K.V., Dvoretskiy, K.N., Chernavina, M.L., Genina, E.A., Genin, V.D., Kochubey, V.I., Lazareva, E.N., Pravdin, A.B., Shvachkina,

M.E., et al. (2018). Measurement of tissue optical properties in the context of tissue optical clearing. J. Biomed. Opt. *23*, 1–31.

Baumgart, E., and Kubitscheck, U. (2012). Scanned light sheet microscopy with confocal slit detection. Opt. Express *20*, 21805–21814.

Bayless, D.W., and Shah, N.M. (2016). Genetic dissection of neural circuits underlying sexually dimorphic social behaviours. Philos. Trans. R. Soc. Lond. B Biol. Sci. *371*, 20150109.

Becker, K., Jährling, N., Saghafi, S., Weiler, R., and Dodt, H.U. (2012). Chemical clearing and dehydration of GFP expressing mouse brains. PLoS ONE *7*, e33916.

Becker, K., Hahn, C.M., Saghafi, S., Jährling, N., Wanis, M., and Dodt, H.U. (2014). Reduction of photo bleaching and long term archiving of chemically cleared GFP-expressing mouse brains. PLoS ONE *9*, e114149.

Belle, M., Godefroy, D., Dominici, C., Heitz-Marchaland, C., Zelina, P., Hellal, F., Bradke, F., and Chédotal, A. (2014). A simple method for 3D analysis of immunolabeled axonal tracts in a transparent nervous system. Cell Rep. *9*, 1191–1201.

Belle, M., Godefroy, D., Couly, G., Malone, S.A., Collier, F., Giacobini, P., and Chédotal, A. (2017). Tridimensional Visualization and Analysis of Early Human Development. Cell *169*, 161–173.

Beltz, B.S., and Kravitz, E.A. (1983). Mapping of serotonin-like immunoreactivity in the lobster nervous system. J. Neurosci. *3*, 585–602.

Bishop, C.A., and O'Shea, M. (1982). Neuropeptide proctolin (H-Arg-Try-Leu-Pro-Thr-OH): immunocytochemical mapping of neurons in the central nervous system of the cockroach. J. Comp. Neurol. *207*, 223–238.

Bouchard, M.B., Voleti, V., Mendes, C.S., Lacefield, C., Grueber, W.B., Mann, R.S., Bruno, R.M., and Hillman, E.M. (2015). Swept confocally-aligned planar excitation (SCAPE) microscopy for high speed volumetric imaging of behaving organisms. Nat. Photonics *9*, 113–119.

Breuninger, T., Greger, K., and Stelzer, E.H. (2007). Lateral modulation boosts image quality in single plane illumination fluorescence microscopy. Opt. Lett. *32*, 1938–1940.

Cai, R., Pan, C., Ghasemigharagoz, A., Todorov, M.I., Förstera, B., Zhao, S., Bhatia, H.S., Mrowka, L., Theodorou, D., et al. (2018). Panoptic vDISCO imaging reveals neuronal connectivity, remote trauma effects and meningeal vessels in intact transparent mice. bioRxiv. https://doi.org/10.1101/374785.

Cai, R., Pan, C., Ghasemigharagoz, A., Todorov, M.I., Förstera, B., Zhao, S., Bhatia, H.S., Parra-Damas, A., Mrowka, L., Theodorou, D., et al. (2019). Panoptic imaging of transparent mice reveals whole-body neuronal projections and skull-meninges connections. Nat. Neurosci. *22*, 317–327.

Cembrowski, M.S., Phillips, M.G., DiLisio, S.F., Shields, B.C., Winnubst, J., Chandrashekar, J., Bas, E., and Spruston, N. (2018). Dissociable Structural and Functional Hippocampal Outputs via Distinct Subiculum Cell Classes. Cell *173*, 1280–1292.e18.

Chakraborty, T., Driscoll, M., Murphy, M., Roudot, P., Chang, B.-J., Vora, S., Wong, W.M., Nielson, C., Zhang, H., Zhemkov, V., et al. (2019). Light-sheet microscopy with isotropic, sub-micron resolution and solvent-independent large-scale imaging. bioRxiv. https://doi.org/10.1101/605493.

Chance, B., Liu, H., Kitai, T., and Zhang, Y. (1995). Effects of solutes on optical properties of biological materials: models, cells, and tissues. Anal. Biochem. *227*, 351–362.

Chen, B.C., Legant, W.R., Wang, K., Shao, L., Milkie, D.E., Davidson, M.W., Janetopoulos, C., Wu, X.S., Hammer, J.A., 3rd, Liu, Z., et al. (2014). Lattice light-sheet microscopy: imaging molecules to embryos at high spatiotemporal resolution. Science *346*, 1257998.

Chen, F., Tillberg, P.W., and Boyden, E.S. (2015). Optical imaging. Expansion microscopy. Science *347*, 543–548.

Chen, L., Li, G., Li, Y., Li, Y., Zhu, H., Tang, L., French, P., McGinty, J., and Ruan, S. (2017). UbasM: An effective balanced optical clearing method for intact biomedical imaging. Sci. Rep. *7*, 12218.

Chhetri, R.K., Amat, F., Wan, Y., Höckendorf, B., Lemon, W.C., and Keller, P.J. (2015). Whole-animal functional and developmental imaging with isotropic spatial resolution. Nat. Methods *12*, 1171–1178.

Chiang, A.S., Liu, Y.C., Chiu, S.L., Hu, S.H., Huang, C.Y., and Hsieh, C.H. (2001). Three-dimensional mapping of brain neuropils in the cockroach, *Diploptera punctata*. J. Comp. Neurol. *440*, 1–11.

Chung, K., Wallace, J., Kim, S.Y., Kalyanasundaram, S., Andalman, A.S., Davidson, T.J., Mirzabekov, J.J., Zalocusky, K.A., Mattis, J., Denisin, A.K., et al. (2013). Structural and molecular interrogation of intact biological systems. Nature *497*, 332–337.

Costantini, I., Ghobril, J.P., Di Giovanna, A.P., Allegra Mascaro, A.L., Silvestri, L., Müllenbroich, M.C., Onofri, L., Conti, V., Vanzi, F., Sacconi, L., et al. (2015). A versatile clearing agent for multi-modal brain imaging. Sci. Rep. *5*, 9808.

Coutu, D.L., Kokkaliaris, K.D., Kunz, L., and Schroeder, T. (2018). Multicolor quantitative confocal imaging cytometry. Nat. Methods *15*, 39–46.

de Medeiros, G., Norlin, N., Gunther, S., Albert, M., Panavaite, L., Fiuza, U.M., Peri, F., Hiiragi, T., Krzic, U., and Hufnagel, L. (2015). Confocal multiview light-sheet microscopy. Nat. Commun. *6*, 8881.

Dean, K.M., Roudot, P., Welf, E.S., Danuser, G., and Fiolka, R. (2015). Deconvolution-free subcellular imaging with axially swept light sheet microscopy. Biophys. J. *108*, 2807–2815.

Dent, J.A., Polson, A.G., and Klymkowsky, M.W. (1989). A whole-mount immunocytochemical analysis of the expression of the intermediate filament protein vimentin in *Xenopus*. Development *105*, 61–74.

Dodt, H.U., Leischner, U., Schierloh, A., Jährling, N., Mauch, C.P., Deininger, K., Deussing, J.M., Eder, M., Zieglgänsberger, W., and Becker, K. (2007). Ultramicroscopy: three-dimensional visualization of neuronal networks in the whole mouse brain. Nat. Methods *4*, 331–336.

Dodt, H.U., Saghafi, S., Becker, K., Jährling, N., Hahn, C., Pende, M., Wanis, M., and Niendorf, A. (2015). Ultramicroscopy: development and outlook. Neurophotonics *2*, 041407.

Dong, H.W. (2008). Allen Reference Atlas. A Digital Color Brain Atlas of the C57BL/6J Male Mouse (John Wiley & Sons).

Dunsby, C. (2008). Optically sectioned imaging by oblique plane microscopy. Opt. Express *16*, 20306–20316.

Duve, H., Thorpe, A., and Strausfeld, N.J. (1983). Cobalt-immunocytochemical identification of peptidergic neurons in Calliphora innervating central and peripheral targets. J. Neurocytol. *12*, 847–861.

Economo, M.N., Clack, N.G., Lavis, L.D., Gerfen, C.R., Svoboda, K., Myers, E.W., and Chandrashekar, J. (2016). A platform for brain-wide imaging and reconstruction of individual neurons. eLife *5*, e10566.

Economo, M.N., Viswanathan, S., Tasic, B., Bas, E., Winnubst, J., Menon, V., Graybuck, L.T., Nguyen, T.N., Smith, K.A., Yao, Z., et al. (2018). Distinct descending motor cortex pathways and their roles in movement. Nature *563*, 79–84.

Economo, M.N., Winnubst, J., Bas, E., Ferreira, T.A., and Chandrashekar, J. (2019). Single-neuron axonal reconstruction: The search for a wiring diagram of the brain. J. Comp. Neurol. *527*, 2190–2199.

Epp, J.R., Niibori, Y., Liz Hsiang, H.L., Mercaldo, V., Deisseroth, K., Josselyn, S.A., and Frankland, P.W. (2015). Optimization of CLARITY for Clearing Whole-Brain and Other Intact Organs. eNeuro *2*, ENEURO.0022-15.2015.

Ertürk, A., Becker, K., Jährling, N., Mauch, C.P., Hojer, C.D., Egen, J.G., Hellal, F., Bradke, F., Sheng, M., and Dodt, H.U. (2012). Three-dimensional imaging of solvent-cleared organs using 3DISCO. Nat. Protoc. *7*, 1983–1995.

Ertürk, A., Lafkas, D., and Chalouni, C. (2014). Imaging cleared intact biological systems at a cellular level by 3DISCO. J. Vis. Exp. *89*, e51382.

Fahrbach, F.O., and Rohrbach, A. (2010). A line scanned light-sheet microscope with phase shaped self-reconstructing beams. Opt. Express *18*, 24229–24244.

Fahrbach, F.O., and Rohrbach, A. (2012). Propagation stability of self-reconstructing Bessel beams enables contrast-enhanced imaging in thick media. Nat. Commun. *3*, 632.

Fahrbach, F.O., Voigt, F.F., Schmid, B., Helmchen, F., and Huisken, J. (2013). Rapid 3D light-sheet microscopy with a tunable lens. Opt. Express *21*, 21010–21026.

Fu, Q., Martin, B.L., Matus, D.Q., and Gao, L. (2016). Imaging multicellular specimens with real-time optimized tiling light-sheet selective plane illumination microscopy. Nat. Commun. *7*, 11088.

Fuchs, E., Jaffe, J., Long, R., and Azam, F. (2002). Thin laser light sheet microscope for microbial oceanography. Opt. Express *10*, 145–154.

Glaser, J.R., and Glaser, E.M. (2000). Stereology, morphometry, and mapping: the whole is greater than the sum of its parts. J. Chem. Neuroanat. *20*, 115–126.

Gleave, J.A., Lerch, J.P., Henkelman, R.M., and Nieman, B.J. (2013). A method for 3D immunostaining and optical imaging of the mouse brain demonstrated in neural progenitor cells. PLoS ONE *8*, e72039.

Gonchar, Y., Wang, Q., and Burkhalter, A. (2008). Multiple distinct subtypes of GABAergic neurons in mouse visual cortex identified by triple immunostaining. Front. Neuroanat. *1*, 3.

Gong, H., Xu, D., Yuan, J., Li, X., Guo, C., Peng, J., Li, Y., Schwarz, L.A., Li, A., Hu, B., et al. (2016). High-throughput dual-colour precision imaging for brain-wide connectome with cytoarchitectonic landmarks at the cellular level. Nat. Commun. *7*, 12142.

Gradinaru, V., Treweek, J., Overton, K., and Deisseroth, K. (2018). Hydrogel-tissue chemistry: Principles and applications. Annu. Rev. Biophys. *47*, 355–376.

Greenbaum, A., Chan, K.Y., Dobreva, T., Brown, D., Balani, D.H., Boyce, R., Kronenberg, H.M., McBride, H.J., and Gradinaru, V. (2017a). Bone CLARITY: Clearing, imaging, and computational analysis of osteoprogenitors within intact bone marrow. Sci. Transl. Med. *9*, eaah6518.

Greenbaum, A., Jang, M.J., Challis, C., and Gradinaru, V. (2017b). Q&A: How can advances in tissue clearing and optogenetics contribute to our understanding of normal and diseased biology? BMC Biol. *15*, 87.

Greer, C.J., and Holy, T.E. (2019). Fast objective coupled planar illumination microscopy. Nat. Commun. *10*, 4483.

Hahn, C., Becker, K., Saghafi, S., Pende, M., Avdibašić, A., Foroughipour, M., Heinz, D.E., Wotjak, C.T., and Dodt, H.-U. (2019). High-resolution imaging of fluorescent whole mouse brains using stabilised organic media (sDISCO). J. Biophotonics *12*, e201800368.

Hama, H., Kurokawa, H., Kawano, H., Ando, R., Shimogori, T., Noda, H., Fukami, K., Sakaue-Sawano, A., and Miyawaki, A. (2011). Sca*l*e: a chemical approach for fluorescence imaging and reconstruction of transparent mouse brain. Nat. Neurosci. *14*, 1481–1488.

Hama, H., Hioki, H., Namiki, K., Hoshida, T., Kurokawa, H., Ishidate, F., Kaneko, T., Akagi, T., Saito, T., Saido, T., and Miyawaki, A. (2015). Sca*l*eS: an optical clearing palette for biological imaging. Nat. Neurosci. *18*, 1518–1529.

Han, Y., Kebschull, J.M., Campbell, R.A.A., Cowan, D., Imhof, F., Zador, A.M., and Mrsic-Flogel, T.D. (2018). The logic of single-cell projections from visual cortex. Nature *556*, 51–56.

Hasegawa, J., Sakamoto, Y., Nakagami, S., Aida, M., Sawa, S., and Matsunaga, S. (2016). Three-dimensional imaging of plant organs using a simple and rapid transparency technique. Plant Cell Physiol. *57*, 462–472.

Hasegawa, S., Susaki, E.A., Tanaka, T., Komaba, H., Wada, T., Fukagawa, M., Ueda, H.R., and Nangaku, M. (2019). Comprehensive three-dimensional analysis (CUBIC-kidney) visualizes abnormal renal sympathetic nerves after ischemia/reperfusion injury. Kidney Int. *96*, 129–138.

Hawrylycz, M., Baldock, R.A., Burger, A., Hashikawa, T., Johnson, G.A., Martone, M., Ng, L., Lau, C., Larson, S.D., Nissanov, J., et al. (2011). Digital atlasing and standardization in the mouse brain. PLoS Comput. Biol. *7*, e1001065.

Herculano-Houzel, S., Watson, C., and Paxinos, G. (2013). Distribution of neurons in functional areas of the mouse cerebral cortex reveals quantitatively different cortical zones. Front. Neuroanat. *7*, 35.

Herculano-Houzel, S., Catania, K., Manger, P.R., and Kaas, J.H. (2015a). Mammalian Brains Are Made of These: A Dataset of the Numbers and Densities of Neuronal and Nonneuronal Cells in the Brain of Glires, Primates, Scandentia, Eulipotyphlans, Afrotherians and Artiodactyls, and Their Relationship with Body Mass. Brain Behav. Evol. *86*, 145–163.

Herculano-Houzel, S., von Bartheld, C.S., Miller, D.J., and Kaas, J.H. (2015b). How to count cells: the advantages and disadvantages of the isotropic fractionator compared with stereology. Cell Tissue Res. *360*, 29–42.

Hildebrand, S., Schueth, A., Herrler, A., Galuske, R., and Roebroeck, A. (2018). Scalable cytoarchitectonic characterization of large intact human neocortex samples. bioRxiv. https://doi.org/10.1101/274985.

Hirshburg, J., Choi, B., Nelson, J.S., and Yeh, A.T. (2007). Correlation between collagen solubility and skin optical clearing using sugars. Lasers Surg. Med. *39*, 140–144.

Holekamp, T.F., Turaga, D., and Holy, T.E. (2008). Fast three-dimensional fluorescence imaging of activity in neural populations by objective-coupled planar illumination microscopy. Neuron *57*, 661–672.

Hooks, B.M., Papale, A.E., Paletzki, R.F., Feroze, M.W., Eastwood, B.S., Couey, J.J., Winnubst, J., Chandrashekar, J., and Gerfen, C.R. (2018). Topographic precision in sensory and motor corticostriatal projections varies across cell type and cortical area. Nat. Commun. *9*, 3549.

Hörl, D., Rojas Rusak, F., Preusser, F., Tillberg, P., Randel, N., Chhetri, R.K., Cardona, A., Keller, P.J., Harz, H., Leonhardt, H., et al. (2018). BigStitcher: Reconstructing high-resolution image datasets of cleared and expanded samples. bioRxiv. https://doi.org/10.1101/343954.

Hou, B., Zhang, D., Zhao, S., Wei, M., Yang, Z., Wang, S., Wang, J., Zhang, X., Liu, B., Fan, L., et al. (2015). Scalable and DiI-compatible optical clearance of the mammalian brain. Front. Neuroanat. *9*, 19.

Hsueh, B., Burns, V.M., Pauerstein, P., Holzem, K., Ye, L., Engberg, K., Wang, A.C., Gu, X., Chakravarthy, H., Arda, H.E., et al. (2017). Pathways to clinical CLARITY: volumetric analysis of irregular, soft, and heterogeneous tissues in development and disease. Sci. Rep. *7*, 5899.

Huang, Z.J. (2014). Toward a genetic dissection of cortical circuits in the mouse. Neuron *83*, 1284–1302.

Huang, Z.J., and Zeng, H. (2013). Genetic approaches to neural circuits in the mouse. Annu. Rev. Neurosci. *36*, 183–215.

Huisken, J., and Stainier, D.Y. (2007). Even fluorescence excitation by multidirectional selective plane illumination microscopy (mSPIM). Opt. Lett. *32*, 2608–2610.

Huisken, J., Swoger, J., Del Bene, F., Wittbrodt, J., and Stelzer, E.H. (2004). Optical sectioning deep inside live embryos by selective plane illumination microscopy. Science *305*, 1007–1009.

Inagaki, T., Hamm, R.N., Arakawa, E.T., and Painter, L.R. (1974). Optical and dielectric properties of DNA in the extreme ultraviolet. J. Chem. Phys. *61*, 4246–4250.

Inoue, M., Saito, R., Kakita, A., and Tainaka, K. (2019). Rapid chemical clearing of white matter in the post-mortem human brain by 1,2-hexanediol delipidation. Bioorg. Med. Chem. Lett. *29*, 1886–1890.

Jing, D., Zhang, S., Luo, W., Gao, X., Men, Y., Ma, C., Liu, X., Yi, Y., Bugde, A., Zhou, B.O., et al. (2018). Tissue clearing of both hard and soft tissue organs with the PEGASOS method. Cell Res. *28*, 803–818.

Jorand, R., Le Corre, G., Andilla, J., Maandhui, A., Frongia, C., Lobjois, V., Ducommun, B., and Lorenzo, C. (2012). Deep and clear optical imaging of thick inhomogeneous samples. PLoS ONE *7*, e35795.

Kawashima, T., Zwart, M.F., Yang, C.T., Mensh, B.D., and Ahrens, M.B. (2016). The Serotonergic System Tracks the Outcomes of Actions to Mediate Short-Term Motor Learning. Cell *167*, 933–946.e20.

Ke, M.-T., Fujimoto, S., and Imai, T. (2013). SeeDB: a simple and morphology-preserving optical clearing agent for neuronal circuit reconstruction. Nat. Neurosci. *16*, 1154–1161.

Ke, M.-T., Nakai, Y., Fujimoto, S., Takayama, R., Yoshida, S., Kitajima, T.S., Sato, M., and Imai, T. (2016). Super-resolution mapping of neuronal circuitry with an index-optimized clearing agent. Cell Rep. *14*, 2718–2732.

Keller, P.J., and Dodt, H.U. (2012). Light sheet microscopy of living or cleared specimens. Curr. Opin. Neurobiol. *22*, 138–143.

Keller, P.J., Schmidt, A.D., Wittbrodt, J., and Stelzer, E.H.K. (2008). Reconstruction of zebrafish early embryonic development by scanned light sheet microscopy. Science *322*, 1065–1069.

Keller, P.J., Schmidt, A.D., Santella, A., Khairy, K., Bao, Z., Wittbrodt, J., and Stelzer, E.H.K. (2010). Fast, high-contrast imaging of animal development with scanned light sheet-based structured-illumination microscopy. Nat. Methods *7*, 637–642.

Kienle, D.F., de Souza, J.V., Watkins, E.B., and Kuhl, T.L. (2014). Thickness and refractive index of DPPC and DPPE monolayers by multiple-beam interferometry. Anal. Bioanal. Chem. *406*, 4725–4733.

Kim, S.Y., Cho, J.H., Murray, E., Bakh, N., Choi, H., Ohn, K., Ruelas, L., Hubbert, A., McCue, M., Vassallo, S.L., et al. (2015a). Stochastic electrotransport selectively enhances the transport of highly electromobile molecules. Proc. Natl. Acad. Sci. USA *112*, E6274–E6283.

Kim, Y., Venkataraju, K.U., Pradhan, K., Mende, C., Taranda, J., Turaga, S.C., Arganda-Carreras, I., Ng, L., Hawrylycz, M.J., Rockland, K.S., et al. (2015b). Mapping social behavior-induced brain activation at cellular resolution in the mouse. Cell Rep. *10*, 292–305.

Kim, Y., Yang, G.R., Pradhan, K., Venkataraju, K.U., Bota, M., Garcia Del Molino, L.C., Fitzgerald, G., Ram, K., He, M., Levine, J.M., et al. (2017). Brain-wide Maps Reveal Stereotyped Cell-Type-Based Cortical Architecture and Subcortical Sexual Dimorphism. Cell *171*, 456–469.

Klingberg, A., Hasenberg, A., Ludwig-Portugall, I., Medyukhina, A., Männ, L., Brenzel, A., Engel, D.R., Figge, M.T., Kurts, C., and Gunzer, M. (2017). Fully automated evaluation of total glomerular number and capillary tuft size in nephritic kidneys using lightsheet microscopy. J. Am. Soc. Nephrol. *28*, 452–459.

Krzic, U., Gunther, S., Saunders, T.E., Streichan, S.J., and Hufnagel, L. (2012). Multiview light-sheet microscope for rapid *in toto* imaging. Nat. Methods *9*, 730–733.

Ku, T., Swaney, J., Park, J.Y., Albanese, A., Murray, E., Cho, J.H., Park, Y.G., Mangena, V., Chen, J., and Chung, K. (2016). Multiplexed and scalable super-resolution imaging of three-dimensional protein localization in size-adjustable tissues. Nat. Biotechnol. *34*, 973–981.

Kuan, L., Li, Y., Lau, C., Feng, D., Bernard, A., Sunkin, S.M., Zeng, H., Dang, C., Hawrylycz, M., and Ng, L. (2015). Neuroinformatics of the allen mouse brain connectivity atlas. Methods *73*, 4–17.

Kubota, S.I., Takahashi, K., Nishida, J., Morishita, Y., Ehata, S., Tainaka, K., Miyazono, K., and Ueda, H.R. (2017). Whole-body profiling of cancer metastasis with single-cell resolution. Cell Rep. *20*, 236–250.

Kumar, V., Scandella, E., Danuser, R., Onder, L., Nitschké, M., Fukui, Y., Halin, C., Ludewig, B., and Stein, J.V. (2010). Global lymphoid tissue remodeling during a viral infection is orchestrated by a B cell-lymphotoxin-dependent pathway. Blood *115*, 4725–4733.

Kurihara, D., Mizuta, Y., Sato, Y., and Higashiyama, T. (2015). ClearSee: a rapid optical clearing reagent for whole-plant fluorescence imaging. Development *142*, 4168–4179.

Kuwajima, T., Sitko, A.A., Bhansali, P., Jurgens, C., Guido, W., and Mason, C. (2013). *Clear*^{T}: a detergent- and solvent-free clearing method for neuronal and non-neuronal tissue. Development *140*, 1364–1368.

Kverková, K., Bělíková, T., Olkowicz, S., Pavelková, Z., O'Riain, M.J., Šumbera, R., Burda, H., Bennett, N.C., and Němec, P. (2018). Sociality does not drive the evolution of large brains in eusocial African mole-rats. Sci. Rep. *8*, 9203.

Lai, H.M., Liu, A.K.L., Ng, W.-L., DeFelice, J., Lee, W.S., Li, H., Li, W., Ng, H.M., Chang, R.C.-C., Lin, B., et al. (2016). Rationalisation and validation of an acrylamide-free procedure in three-dimensional histological imaging. PLoS ONE *11*, e0158628.

Lai, H.M., Liu, A.K.L., Ng, H.H.M., Goldfinger, M.H., Chau, T.W., DeFelice, J., Tilley, B.S., Wong, W.M., Wu, W., and Gentleman, S.M. (2018). Next generation histology methods for three-dimensional imaging of fresh and archival human brain tissues. Nat. Commun. *9*, 1066.

Lee, H., Park, J.H., Seo, I., Park, S.H., and Kim, S. (2014). Improved application of the electrophoretic tissue clearing technology, CLARITY, to intact solid organs including brain, pancreas, liver, kidney, lung, and intestine. BMC Dev. Biol. *14*, 48.

Lee, E., Choi, J., Jo, Y., Kim, J.Y., Jang, Y.J., Lee, H.M., Kim, S.Y., Lee, H.-J., Cho, K., Jung, N., et al. (2016). ACT-PRESTO: Rapid and consistent tissue clearing and labeling method for 3-dimensional (3D) imaging. Sci. Rep. *6*, 18631.

Lein, E.S., Hawrylycz, M.J., Ao, N., Ayres, M., Bensinger, A., Bernard, A., Boe, A.F., Boguski, M.S., Brockway, K.S., Byrnes, E.J., et al. (2007). Genome-wide atlas of gene expression in the adult mouse brain. Nature *445*, 168–176.

Lemon, W.C., Pulver, S.R., Höckendorf, B., McDole, K., Branson, K., Freeman, J., and Keller, P.J. (2015). Whole-central nervous system functional imaging in larval *Drosophila*. Nat. Commun. *6*, 7924.

Li, A., Gong, H., Zhang, B., Wang, Q., Yan, C., Wu, J., Liu, Q., Zeng, S., and Luo, Q. (2010). Micro-optical sectioning tomography to obtain a high-resolution atlas of the mouse brain. Science *330*, 1404–1408.

Li, W., Germain, R.N., and Gerner, M.Y. (2017). Multiplex, quantitative cellular analysis in large tissue volumes with clearing-enhanced 3D microscopy (C_e3D). Proc. Natl. Acad. Sci. USA *114*, E7321–E7330.

Li, X., Yu, B., Sun, Q., Zhang, Y., Ren, M., Zhang, X., Li, A., Yuan, J., Madisen, L., Luo, Q., et al. (2018). Generation of a whole-brain atlas for the cholinergic system and mesoscopic projectome analysis of basal forebrain cholinergic neurons. Proc. Natl. Acad. Sci. USA *115*, 415–420.

Liebmann, T., Renier, N., Bettayeb, K., Greengard, P., Tessier-Lavigne, M., and Flajolet, M. (2016). Three-dimensional study of Alzheimer's disease hallmarks using the idisco clearing method. Cell Rep. *16*, 1138–1152.

Liu, H., Beauvoit, B., Kimura, M., and Chance, B. (1996). Dependence of tissue optical properties on solute-induced changes in refractive index and osmolarity. J. Biomed. Opt. *1*, 200–211.

Liu, A.K.L., Hurry, M.E., Ng, O.T.-W., DeFelice, J., Lai, H.M., Pearce, R.K., Wong, G.T.C., Chang, R.C.C., and Gentleman, S.M. (2016). Bringing CLARITY to the human brain: visualization of Lewy pathology in three dimensions. Neuropathol. Appl. Neurobiol. *42*, 573–587.

Liu, T.L., Upadhyayula, S., Milkie, D.E., Singh, V., Wang, K., Swinburne, I.A., Mosaliganti, K.R., Collins, Z.M., Hiscock, T.W., Shea, J., et al. (2018). Observing the cell in its native state: Imaging subcellular dynamics in multicellular organisms. Science *360*, eaaq1392.

Lorentz, H.A. (1880). Ueber die Beziehung zwischen der Fortpflanzungsgeschwindigkeit des Lichtes und der Körperdichte. Ann. Phys. *245*, 641–665.

Lorenz, L. (1880). Über die Refractionsconstante. Ann. Phys. *247*, 70–103.

Madisen, L., Mao, T., Koch, H., Zhuo, J.M., Berenyi, A., Fujisawa, S., Hsu, Y.W., Garcia, A.J., 3rd, Gu, X., Zanella, S., et al. (2012). A toolbox of Cre-dependent optogenetic transgenic mice for light-induced activation and silencing. Nat. Neurosci. *15*, 793–802.

Mahou, P., Vermot, J., Beaurepaire, E., and Supatto, W. (2014). Multicolor two-photon light-sheet microscopy. Nat. Methods *11*, 600–601.

Marhounová, L., Kotrschal, A., Kverková, K., Kolm, N., and Němec, P. (2019). Artificial selection on brain size leads to matching changes in overall number of neurons. Evolution *73*, 2003–2012.

Matsumoto, K., Mitani, T.T., Horiguchi, S.A., Kaneshiro, J., Murakami, T.C., Mano, T., Fujishima, H., Konno, A., Watanabe, T.M., Hirai, H., and Ueda, H.R. (2019). Advanced CUBIC tissue clearing for whole-organ cell profiling. Nat. Protoc. *14*, 3506–3537.

Mayerich, D., Abbott, L., and McCormick, B. (2008). Knife-edge scanning microscopy for imaging and reconstruction of three-dimensional anatomical structures of the mouse brain. J. Microsc. *231*, 134–143.

McDole, K., Guignard, L., Amat, F., Berger, A., Malandain, G., Royer, L.A., Turaga, S.C., Branson, K., and Keller, P.J. (2018). *In Toto* Imaging and Reconstruction of Post-Implantation Mouse Development at the Single-Cell Level. Cell *175*, 859–876.e33.

McGorty, R., Liu, H., Kamiyama, D., Dong, Z., Guo, S., and Huang, B. (2015). Open-top selective plane illumination microscope for conventionally mounted specimens. Opt. Express *23*, 16142–16153.

Migliori, B., Datta, M.S., Dupre, C., Apak, M.C., Asano, S., Gao, R., Boyden, E.S., Hermanson, O., Yuste, R., and Tomer, R. (2018). Light sheet theta microscopy for rapid high-resolution imaging of large biological samples. BMC Biol. *16*, 57.

Mitra, P.P. (2014). The circuit architecture of whole brains at the mesoscopic scale. Neuron *83*, 1273–1283.

Mizutani, H., Ono, S., Ushiku, T., Kudo, Y., Ikemura, M., Kageyama, N., Yamamichi, N., Fujishiro, M., Someya, T., Fukayama, M., et al. (2018). Transparency-enhancing technology allows three-dimensional assessment of gastrointestinal mucosa: A porcine model. Pathol. Int. *68*, 102–108.

Murakami, T.C., Mano, T., Saikawa, S., Horiguchi, S.A., Shigeta, D., Baba, K., Sekiya, H., Shimizu, Y., Tanaka, K.F., Kiyonari, H., et al. (2018). A three-dimensional single-cell-resolution whole-brain atlas using CUBIC-X expansion microscopy and tissue clearing. Nat. Neurosci. *21*, 625–637.

Murray, E., Cho, J.H., Goodwin, D., Ku, T., Swaney, J., Kim, S.Y., Choi, H., Park, Y.G., Park, J.Y., Hubbert, A., et al. (2015). Simple, Scalable Proteomic Imaging for High-Dimensional Profiling of Intact Systems. Cell *163*, 1500–1514.

Ng, L., Pathak, S.D., Kuan, C., Lau, C., Dong, H., Sodt, A., Dang, C., Avants, B., Yushkevich, P., Gee, J.C., et al. (2007). Neuroinformatics for genome-wide 3D gene expression mapping in the mouse brain. IEEE/ACM Trans. Comput. Biol. Bioinformatics *4*, 382–393.

Nixon-Abell, J., Obara, C.J., Weigel, A.V., Li, D., Legant, W.R., Xu, C.S., Pasolli, H.A., Harvey, K., Hess, H.F., Betzig, E., et al. (2016). Increased spatiotemporal resolution reveals highly dynamic dense tubular matrices in the peripheral ER. Science *354*, aaf3928.

Nojima, S., Susaki, E.A., Yoshida, K., Takemoto, H., Tsujimura, N., Iijima, S., Takachi, K., Nakahara, Y., Tahara, S., Ohshima, K., et al. (2017). CUBIC pathology: three-dimensional imaging for pathological diagnosis. Sci. Rep. *7*, 9269.

Ogawa, S.K., and Watabe-Uchida, M. (2018). Organization of dopamine and serotonin system: Anatomical and functional mapping of monosynaptic inputs using rabies virus. Pharmacol. Biochem. Behav. *174*, 9–22.

Oh, S.W., Harris, J.A., Ng, L., Winslow, B., Cain, N., Mihalas, S., Wang, Q., Lau, C., Kuan, L., Henry, A.M., et al. (2014). A mesoscale connectome of the mouse brain. Nature *508*, 207–214.

Olarte, O.E., Andilla, J., Artigas, D., and Loza-Alvarez, P. (2015). Decoupled illumination detection in light sheet microscopy for fast volumetric imaging. Optica *2*, 702–705.

Olkowicz, S., Kocourek, M., Lučan, R.K., Porteš, M., Fitch, W.T., Herculano-Houzel, S., and Němec, P. (2016). Birds have primate-like numbers of neurons in the forebrain. Proc. Natl. Acad. Sci. USA *113*, 7255–7260.

Osten, P., and Margrie, T.W. (2013). Mapping brain circuitry with a light microscope. Nat. Methods *10*, 515–523.

Palero, J., Santos, S.I., Artigas, D., and Loza-Alvarez, P. (2010). A simple scanless two-photon fluorescence microscope using selective plane illumination. Opt. Express *18*, 8491–8498.

Palmer, W.M., Martin, A.P., Flynn, J.R., Reed, S.L., White, R.G., Furbank, R.T., and Grof, C.P.L. (2015). PEA-CLARITY: 3D molecular imaging of whole plant organs. Sci. Rep. *5*, 13492.

Pan, C., Cai, R., Quacquarelli, F.P., Ghasemigharagoz, A., Lourbopoulos, A., Matryba, P., Plesnila, N., Dichgans, M., Hellal, F., and Ertürk, A. (2016). Shrinkage-mediated imaging of entire organs and organisms using uDISCO. Nat. Methods *13*, 859–867.

Panier, T., Romano, S.A., Olive, R., Pietri, T., Sumbre, G., Candelier, R., and Debrégeas, G. (2013). Fast functional imaging of multiple brain regions in intact zebrafish larvae using selective plane illumination microscopy. Front. Neural Circuits *7*, 65.

Park, Y.-G., Sohn, C.H., Chen, R., McCue, M., Yun, D.H., Drummond, G.T., Ku, T., Evans, N.B., Oak, H.C., Trieu, W., et al. (2018). Protection of tissue physicochemical properties using polyfunctional crosslinkers. Nat. Biotechnol. *37*, 73–83.

Pende, M., Becker, K., Wanis, M., Saghafi, S., Kaur, R., Hahn, C., Pende, N., Foroughipour, M., Hummel, T., and Dodt, H.-U. (2018). High-resolution ultramicroscopy of the developing and adult nervous system in optically cleared *Drosophila melanogaster*. Nat. Commun. *9*, 4731.

Perbellini, F., Liu, A.K.L., Watson, S.A., Bardi, I., Rothery, S.M., and Terracciano, C.M. (2017). Free-of-Acrylamide SDS-based Tissue Clearing (FASTClear) for three dimensional visualization of myocardial tissue. Sci. Rep. *7*, 5188.

Pfeffer, C.K., Xue, M., He, M., Huang, Z.J., and Scanziani, M. (2013). Inhibition of inhibition in visual cortex: the logic of connections between molecularly distinct interneurons. Nat. Neurosci. *16*, 1068–1076.

Piezosystems_Jena. (2019). nanoX 200/400 and nanoSX 400/800. https://www.piezosystem.com/products/piezo_actuators/nanox/.

Planchon, T.A., Gao, L., Milkie, D.E., Davidson, M.W., Galbraith, J.A., Galbraith, C.G., and Betzig, E. (2011). Rapid three-dimensional isotropic imaging of living cells using Bessel beam plane illumination. Nat. Methods *8*, 417–423.

Prönneke, A., Scheuer, B., Wagener, R.J., Möck, M., Witte, M., and Staiger, J.F. (2015). Characterizing VIP Neurons in the Barrel Cortex of VIPcre/tdTomato Mice Reveals Layer-Specific Differences. Cereb. Cortex *25*, 4854–4868.

Pusterla, J.M., Malfatti-Gasperini, A.A., Puentes-Martinez, X.E., Cavalcanti, L.P., and Oliveira, R.G. (2017). Refractive index and thickness determination in Langmuir monolayers of myelin lipids. Biochim. Biophys. Acta Biomembr. *1859*, 924–930.

Quirin, S., Vladimirov, N., Yang, C.-T., Peterka, D.S., Yuste, R., and Ahrens, M.B. (2016). Calcium imaging of neural circuits with extended depth-of-field light-sheet microscopy. Opt. Lett. *41*, 855–858.

Ragan, T., Kadiri, L.R., Venkataraju, K.U., Bahlmann, K., Sutin, J., Taranda, J., Arganda-Carreras, I., Kim, Y., Seung, H.S., and Osten, P. (2012). Serial two-photon tomography for automated *ex vivo* mouse brain imaging. Nat. Methods *9*, 255–258.

Reichmann, J., Nijmeijer, B., Hossain, M.J., Eguren, M., Schneider, I., Politi, A.Z., Roberti, M.J., Hufnagel, L., Hiiragi, T., and Ellenberg, J. (2018). Dual-spindle formation in zygotes keeps parental genomes apart in early mammalian embryos. Science *361*, 189–193.

Renier, N., Wu, Z., Simon, D.J., Yang, J., Ariel, P., and Tessier-Lavigne, M. (2014). iDISCO: a simple, rapid method to immunolabel large tissue samples for volume imaging. Cell *159*, 896–910.

Renier, N., Adams, E.L., Kirst, C., Wu, Z., Azevedo, R., Kohl, J., Autry, A.E., Kadiri, L., Umadevi Venkataraju, K., Zhou, Y., et al. (2016). Mapping of brain activity by automated volume analysis of immediate early genes. Cell *165*, 1789–1802.

Richardson, D.S., and Lichtman, J.W. (2015). Clarifying Tissue Clearing. Cell *162*, 246–257.

Royer, L.A., Lemon, W.C., Chhetri, R.K., Wan, Y., Coleman, M., Myers, E.W., and Keller, P.J. (2016). Adaptive light-sheet microscopy for long-term, high-resolution imaging in living organisms. Nat. Biotechnol. *34*, 1267–1278.

Rozbicki, E., Chuai, M., Karjalainen, A.I., Song, F., Sang, H.M., Martin, R., Knölker, H.J., MacDonald, M.P., and Weijer, C.J. (2015). Myosin-II-mediated cell shape changes and cell intercalation contribute to primitive streak formation. Nat. Cell Biol. *17*, 397–408.

Rudy, B., Fishell, G., Lee, S., and Hjerling-Leffler, J. (2011). Three groups of interneurons account for nearly 100% of neocortical GABAergic neurons. Dev. Neurobiol. *71*, 45–61.

Saghafi, S., Becker, K., Hahn, C., and Dodt, H.U. (2014). 3D-ultramicroscopy utilizing aspheric optics. J. Biophotonics *7*, 117–125.

Schmid, B., Shah, G., Scherf, N., Weber, M., Thierbach, K., Campos, C.P., Roeder, I., Aanstad, P., and Huisken, J. (2013). High-speed panoramic light-sheet microscopy reveals global endodermal cell dynamics. Nat. Commun. *4*, 2207.

Schmitz, C., and Hof, P.R. (2005). Design-based stereology in neuroscience. Neuroscience *130*, 813–831.

Schwarz, M.K., Scherbarth, A., Sprengel, R., Engelhardt, J., Theer, P., and Giese, G. (2015). Fluorescent-protein stabilization and high-resolution imaging of cleared, intact mouse brains. PLoS ONE *10*, e0124650.

Seiriki, K., Kasai, A., Hashimoto, T., Schulze, W., Niu, M., Yamaguchi, S., Nakazawa, T., Inoue, K.I., Uezono, S., Takada, M., et al. (2017). High-Speed and Scalable Whole-Brain Imaging in Rodents and Primates. Neuron *94*, 1085–1100.e6.

Shah, S., Lubeck, E., Schwarzkopf, M., He, T.F., Greenbaum, A., Sohn, C.H., Lignell, A., Choi, H.M., Gradinaru, V., Pierce, N.A., and Cai, L. (2016). Single-molecule RNA detection at depth by hybridization chain reaction and tissue hydrogel embedding and clearing. Development *143*, 2862–2867.

Sheppard, C.J.R. (2013). Pupil filters for generation of light sheets. Opt. Express *21*, 6339–6345.

Siedentopf, H., and Zsigmondy, R. (1902). Über Sichtbarmachung und Größenbestimmung ultramikoskopischer Teilchen, mit besonderer Anwendung auf Goldrubingläser. Ann. Phys. *315*, 1–39.

Sillitoe, R.V., and Hawkes, R. (2002). Whole-mount immunohistochemistry: a high-throughput screen for patterning defects in the mouse cerebellum. J. Histochem. Cytochem. *50*, 235–244.

Silvestri, L., Bria, A., Sacconi, L., Iannello, G., and Pavone, F.S. (2012). Confocal light sheet microscopy: micron-scale neuroanatomy of the entire mouse brain. Opt. Express *20*, 20582–20598.

Silvestri, L., Costantini, I., Sacconi, L., and Pavone, F.S. (2016). Clearing of fixed tissue: a review from a microscopist's perspective. J. Biomed. Opt. *21*, 081205.

Simerly, R.B. (2002). Wired for reproduction: organization and development of sexually dimorphic circuits in the mammalian forebrain. Annu. Rev. Neurosci. *25*, 507–536.

Spalteholz, W. (1911). Über das Durchsichtigmachen von menschlichen und tierischen Präparaten (S. Hirzel).

Staudt, T., Lang, M.C., Medda, R., Engelhardt, J., and Hell, S.W. (2007). 2,2′-thiodiethanol: a new water soluble mounting medium for high resolution optical microscopy. Microsc. Res. Tech. *70*, 1–9.

Stephan, H., Frahm, H., and Baron, G. (1981). New and revised data on volumes of brain structures in insectivores and primates. Folia Primatol. (Basel) *35*, 1–29.

Strnad, P., Gunther, S., Reichmann, J., Krzic, U., Balazs, B., de Medeiros, G., Norlin, N., Hiiragi, T., Hufnagel, L., and Ellenberg, J. (2016). Inverted light-sheet microscope for imaging mouse pre-implantation development. Nat. Methods *13*, 139–142.

Susaki, E.A., and Ueda, H.R. (2016). Whole-body and Whole-Organ Clearing and Imaging Techniques with Single-Cell Resolution: Toward Organism-Level Systems Biology in Mammals. Cell Chem. Biol. *23*, 137–157.

Susaki, E.A., Tainaka, K., Perrin, D., Kishino, F., Tawara, T., Watanabe, T.M., Yokoyama, C., Onoe, H., Eguchi, M., Yamaguchi, S., et al. (2014). Whole-brain imaging with single-cell resolution using chemical cocktails and computational analysis. Cell *157*, 726–739.

Susaki, E.A., Tainaka, K., Perrin, D., Yukinaga, H., Kuno, A., and Ueda, H.R. (2015). Advanced CUBIC protocols for whole-brain and whole-body clearing and imaging. Nat. Protoc. *10*, 1709–1727.

Swoger, J., Verveer, P., Greger, K., Huisken, J., and Stelzer, E.H. (2007). Multi-view image fusion improves resolution in three-dimensional microscopy. Opt. Express *15*, 8029–8042.

Sylwestrak, E.L., Rajasethupathy, P., Wright, M.A., Jaffe, A., and Deisseroth, K. (2016). Multiplexed Intact-Tissue Transcriptional Analysis at Cellular Resolution. Cell *164*, 792–804.

Tainaka, K., Kubota, S.I., Suyama, T.Q., Susaki, E.A., Perrin, D., Ukai-Tadenuma, M., Ukai, H., and Ueda, H.R. (2014). Whole-body imaging with single-cell resolution by tissue decolorization. Cell *159*, 911–924.

Tainaka, K., Kuno, A., Kubota, S.I., Murakami, T., and Ueda, H.R. (2016). Chemical Principles in Tissue Clearing and Staining Protocols for Whole-Body Cell Profiling. Annu. Rev. Cell Dev. Biol. *32*, 713–741.

Tainaka, K., Murakami, T.C., Susaki, E.A., Shimizu, C., Saito, R., Takahashi, K., Hayashi-Takagi, A., Sekiya, H., Arima, Y., Nojima, S., et al. (2018). Chemical Landscape for Tissue Clearing Based on Hydrophilic Reagents. Cell Rep. *24*, 2196–2210.e9.

Tanaka, N., Kanatani, S., Tomer, R., Sahlgren, C., Kronqvist, P., Kaczynska, D., Louhivuori, L., Kis, L., Lindh, C., Mitura, P., et al. (2017). Whole-tissue biopsy phenotyping of three-dimensional tumours reveals patterns of cancer heterogeneity. Nat. Biomed. Eng. *1*, 796–806.

Tatsuki, F., Sunagawa, G.A., Shi, S., Susaki, E.A., Yukinaga, H., Perrin, D., Sumiyama, K., Ukai-Tadenuma, M., Fujishima, H., Ohno, R., et al. (2016). Involvement of Ca(2+)-Dependent Hyperpolarization in Sleep Duration in Mammals. Neuron *90*, 70–85.

Tomer, R., Khairy, K., Amat, F., and Keller, P.J. (2012). Quantitative high-speed imaging of entire developing embryos with simultaneous multiview light-sheet microscopy. Nat. Methods *9*, 755–763.

Tomer, R., Ye, L., Hsueh, B., and Deisseroth, K. (2014). Advanced CLARITY for rapid and high-resolution imaging of intact tissues. Nat. Protoc. *9*, 1682–1697.

Tomer, R., Lovett-Barron, M., Kauvar, I., Andalman, A., Burns, V.M., Sankaran, S., Grosenick, L., Broxton, M., Yang, S., and Deisseroth, K. (2015). SPED Light Sheet Microscopy: Fast Mapping of Biological System Structure and Function. Cell *163*, 1796–1806.

Treweek, J.B., Chan, K.Y., Flytzanis, N.C., Yang, B., Deverman, B.E., Greenbaum, A., Lignell, A., Xiao, C., Cai, L., Ladinsky, M.S., et al. (2015). Whole-body tissue stabilization and selective extractions via tissue-hydrogel hybrids for high-resolution intact circuit mapping and phenotyping. Nat. Protoc. *10*, 1860–1896.

Truong, T.V., Supatto, W., Koos, D.S., Choi, J.M., and Fraser, S.E. (2011). Deep and fast live imaging with two-photon scanned light-sheet microscopy. Nat. Methods *8*, 757–760.

Tsai, P.S., Kaufhold, J.P., Blinder, P., Friedman, B., Drew, P.J., Karten, H.J., Lyden, P.D., and Kleinfeld, D. (2009). Correlations of neuronal and microvascular densities in murine cortex revealed by direct counting and colocalization of nuclei and vessels. J. Neurosci. *29*, 14553–14570.

Tuchin, V. (2007). Tissue Optics: Light Scattering Methods and Instruments for Medical Diagnosis, Second Edition (SPIE Press).

Tuchin, V.V. (2015). Tissue optics and photonics: light-tissue interaction. J. Biomed. Photonics Eng. *1*, 98–134.

Tuchin, V.V., Maksimova, I.L., Zimnyakov, D.A., Kon, I.L., Mavlyutov, A.H., and Mishin, A.A. (1997). Light propagation in tissues with controlled optical properties. J. Biomed. Opt. *2*, 401–417.

Tuchin, V.V., Xu, X., and Wang, R.K. (2002). Dynamic optical coherence tomography in studies of optical clearing, sedimentation, and aggregation of immersed blood. Appl. Opt. *41*, 258–271.

Valm, A.M., Cohen, S., Legant, W.R., Melunis, J., Hershberg, U., Wait, E., Cohen, A.R., Davidson, M.W., Betzig, E., and Lippincott-Schwartz, J. (2017). Applying systems-level spectral imaging and analysis to reveal the organelle interactome. Nature *546*, 162–167.

Verveer, P.J., Swoger, J., Pampaloni, F., Greger, K., Marcello, M., and Stelzer, E.H. (2007). High-resolution three-dimensional imaging of large specimens with light sheet-based microscopy. Nat. Methods *4*, 311–313.

Vettenburg, T., Dalgarno, H.I., Nylk, J., Coll-Lladó, C., Ferrier, D.E., Čižmár, T., Gunn-Moore, F.J., and Dholakia, K. (2014). Light-sheet microscopy using an Airy beam. Nat. Methods *11*, 541–544.

Voie, A.H., Burns, D.H., and Spelman, F.A. (1993). Orthogonal-plane fluorescence optical sectioning: three-dimensional imaging of macroscopic biological specimens. J. Microsc. *170*, 229–236.

Voigt, F.F., Kirschenbaum, D., Platonova, E., Pagès, S., Campbell, R.A.A., Kastli, R., Schaettin, M., Egolf, L., van der Bourg, A., Bethge, P., et al. (2019). The mesoSPIM initiative: open-source light-sheet microscopes for imaging cleared tissue. Nat. Methods *16*, 1105–1108.

Wan, Y., Wei, Z., Looger, L.L., Koyama, M., Druckmann, S., and Keller, P.J. (2019). Single-Cell Reconstruction of Emerging Population Activity in an Entire Developing Circuit. Cell *179*, 355–372.

Wang, Z., Zhang, J., Fan, G., Zhao, H., Wang, X., Zhang, J., Zhang, P., and Wang, W. (2018). Imaging transparent intact cardiac tissue with single-cell resolution. Biomed. Opt. Express *9*, 423–436.

Wang, Y., Xie, P., Gong, H., Zhou, Z., Kuang, X., Wang, Y., Li, A.-a., Li, Y., Liu, L., Veldman, M.B., et al. (2019). Complete single neuron reconstruction reveals morphological diversity in molecularly defined claustral and cortical neuron types. bioRxiv. https://doi.org/10.1101/675280.

Warner, C.A., Biedrzycki, M.L., Jacobs, S.S., Wisser, R.J., Caplan, J.L., and Sherrier, D.J. (2014). An optical clearing technique for plant tissues allowing deep imaging and compatible with fluorescence microscopy. Plant Physiol. *166*, 1684–1687.

White, J.G., Southgate, E., Thomson, J.N., and Brenner, S. (1986). The structure of the nervous system of the nematode *Caenorhabditis elegans*. Philos. Trans. R. Soc. Lond. B Biol. Sci. *314*, 1–340.

Wilding, D., Pozzi, P., Soloviev, O., Vdovin, G., and Verhaegen, M. (2016). Adaptive illumination based on direct wavefront sensing in a light-sheet fluorescence microscope. Opt. Express *24*, 24896–24906.

Williams, R.W., and Rakic, P. (1988). Three-dimensional counting: an accurate and direct method to estimate numbers of cells in sectioned material. J. Comp. Neurol. *278*, 344–352.

Winnubst, J., Bas, E., Ferreira, T.A., Wu, Z., Economo, M.N., Edson, P., Arthur, B.J., Bruns, C., Rokicki, K., Schauder, D., et al. (2019). Reconstruction of 1,000 projection neurons reveals new cell types and organization of long-range connectivity in the mouse brain. Cell *179*, 268–281.e13.

Wolf, S., Supatto, W., Debrégeas, G., Mahou, P., Kruglik, S.G., Sintes, J.M., Beaurepaire, E., and Candelier, R. (2015). Whole-brain functional imaging with two-photon light-sheet microscopy. Nat. Methods *12*, 379–380.

Wu, Y., Ghitani, A., Christensen, R., Santella, A., Du, Z., Rondeau, G., Bao, Z., Colón-Ramos, D., and Shroff, H. (2011). Inverted selective plane illumination microscopy (iSPIM) enables coupled cell identity lineaging and neurodevelopmental imaging in *Caenorhabditis elegans*. Proc. Natl. Acad. Sci. USA *108*, 17708–17713.

Wu, Y., Wawrzusin, P., Senseney, J., Fischer, R.S., Christensen, R., Santella, A., York, A.G., Winter, P.W., Waterman, C.M., Bao, Z., et al. (2013). Spatially isotropic four-dimensional imaging with dual-view plane illumination microscopy. Nat. Biotechnol. *31*, 1032–1038.

Xu, X., Wang, R.K., Elder, J.B., and Tuchin, V.V. (2003). Effect of dextran-induced changes in refractive index and aggregation on optical properties of whole blood. Phys. Med. Biol. *48*, 1205–1221.

Xu, X., Roby, K.D., and Callaway, E.M. (2010). Immunochemical characterization of inhibitory mouse cortical neurons: three chemically distinct classes of inhibitory cells. J. Comp. Neurol. *518*, 389–404.

Xu, N., Tamadon, A., Liu, Y., Ma, T., Leak, R.K., Chen, J., Gao, Y., and Feng, Y. (2017). Fast free-of-acrylamide clearing tissue (FACT)-an optimized new protocol for rapid, high-resolution imaging of three-dimensional brain tissue. Sci. Rep. *7*, 9895.

Yang, B., Treweek, J.B., Kulkarni, R.P., Deverman, B.E., Chen, C.K., Lubeck, E., Shah, S., Cai, L., and Gradinaru, V. (2014). Single-cell phenotyping within transparent intact tissue through whole-body clearing. Cell *158*, 945–958.

Ye, L., Allen, W.E., Thompson, K.R., Tian, Q., Hsueh, B., Ramakrishnan, C., Wang, A.C., Jennings, J.H., Adhikari, A., Halpern, C.H., et al. (2016). Wiring and Molecular Features of Prefrontal Ensembles Representing Distinct Experiences. Cell *165*, 1776–1788.

Yu, T., Zhu, J., Li, Y., Ma, Y., Wang, J., Cheng, X., Jin, S., Sun, Q., Li, X., Gong, H., et al. (2018). RTF: a rapid and versatile tissue optical clearing method. Sci. Rep. *8*, 1964.

Zhao, S., Todorov, M.I., Cai, R., Steinke, H., Kemter, E., Wolf, E., Lipfert, J., Bechmann, I., and Ertürk, A. (2019). Cellular and Molecular Probing of Intact Transparent Human Organs. bioRxiv. https://doi.org/10.1101/643908.

Zheng, T., Yang, Z., Li, A., Lv, X., Zhou, Z., Wang, X., Qi, X., Li, S., Luo, Q., Gong, H., and Zeng, S. (2013). Visualization of brain circuits using two-photon fluorescence micro-optical sectioning tomography. Opt. Express *21*, 9839–9850.